Electron Emission from Metal Nanotips Driven by Plasma-Generated THz Pulses for Electron Microscopy

Benjamin Colmey

Department of Physics

McGill University

Montréal, Québec, Canada

June 1st, 2024

A thesis submitted in partial fulfillment of the requirements of the degree of Master of Science

Abstract

This thesis details significant progress in electron emission from tungsten nanotips, driven by plasma-generated terahertz (THz) fields, a project undertaken as part of McGill University's Quantum Dynamics Lab. The development of this ultrafast electron source, coupled with the design of a novel point-projection electron microscope and ultra-high vacuum system, represents a significant advancement in the field of electron microscopy.

Using a two-colour air-plasma with a filament length of 5 cm, we detected THz pulses with pulse energies of 186 nJ and full width half maximum (FWHM) at the focus of 350 μm. Initially, using the Poynting flux method, we estimated large field strengths in the range of 700 kV/cm, motivating their use for electron emission. However, upon driving cold field electron emission from tungsten nanotips, we observed electrons with energies of 1.2 keV and bunch charges exceeding 10^5 electrons, indicating field strengths of $\approx$ 160 kV/cm, far weaker than previously estimated. This discrepancy is attributed to poor THz beam collimation, leading to a flying focus and multiple pulses arriving staggered in time.

To address this, we proposed a collimation method using an axicon lens. Early results

showed improvements in the spatial distribution of the focus, achieving a focus FWHM of 200 μm, and a fourfold increase in electric field amplitude measured via EO sampling, with improved field strengths of over 600 kV/cm.

Additionally, we present the design aspects of a novel point-projection electron microscope and its ultrahigh vacuum system, highlighting the simulation of vacuum conditions and conductance analysis of system components, crucial in achieving ultra-high vacuum pressures of 10^{-9} Torr. These pressures are required to study stable surfaces on the atomic scale. These developments, combined with the refinement of our plasma source, lay a robust foundation for the Quantum Dynamics Lab.

Abrégé

Cette thèse détaille des progrès significatifs dans l'émission d'électrons à partir de nanotips en tungstène, générée par des champs térahertz (THz) produits par plasma, un projet entrepris dans le cadre du Quantum Dynamics Lab de l'Université McGill. Le développement de cette source d'électrons ultrarapide, couplé à la conception d'un microscope électronique à projection ponctuelle et d'un système à ultra-haut vide, représente une avancée significative dans le domaine de la microscopie électronique.

En utilisant un plasma d'air à deux couleurs avec une longueur de filament de 5 cm, nous avons détecté des impulsions THz avec des énergies de 186 nJ et une largeur à mi-hauteur au foyer de 350 µm. Initialement, en utilisant la méthode du flux de Poynting, nous avons estimé des intensités de champ importantes de l'ordre de 700 kV/cm, motivant leur utilisation pour l'émission d'électrons. Cependant, en provoquant l'émission d'électrons par champ froid à partir de nanotips en tungstène, nous avons observé des électrons avec des énergies de 1,2 keV et des charges de paquets dépassant 10^5 électrons, indiquant des intensités de champ d'environ 160 kV/cm, bien plus faibles que les estimations précédentes. Cette divergence

est attribuée à une mauvaise collimation du faisceau THz, entraînant l'arrivée décalée de multiples impulsions dans le temps.

Pour remédier cela, nous avons proposé une méthode de collimation utilisant une lentille axicon. Les premiers résultats ont montré des améliorations dans la distribution spatiale du foyer, atteignant une FWHM de 200 µm, et une augmentation quadruplée de l'amplitude du champ électrique mesurée par échantillonnage EO, avec des intensités de champ améliorées de plus de 600 kV/cm.

De plus, nous présentons les aspects de conception d'un nouveau microscope électronique à projection ponctuelle et de son système à ultra-haut vide, en mettant en avant la simulation des conditions de vide et l'analyse de la conductance des composants du système, cruciales pour atteindre des pressions ultra-hautes de 10^{-9} Torr. Ces pressions sont nécessaires pour étudier les surfaces stables à l'échelle atomique. Ces développements, combinés au perfectionnement de notre source plasma, posent une base solide pour le Quantum Dynamics Lab.

Acknowledgements

I would like to thank all current and former members of the Cooke group with whom I have had the pleasure of working. Firstly, thank you to Malte and Rodrigo, for sharing parts of this project and graciously putting up with my choice of lab music. I also want to extend my gratitude to Ben D. and Aidan for their frequent help and friendship. Acknowledgment is further due to Dominique, whose work has propelled all of QDL and laid the foundation for this thesis. Were it not for the detailed documentation left for me, I would not have learned and become the experimentalist I am today. Finally, I would like to thank Dave, for his wisdom and humor, and for showing me physics can be easy, as long as you're a genius.

Contents

List of Figures

List of Acronyms

ABCD	air-biased coherent detection.
BBO	Beta-Barium-Borate.
CFE	cold field emission.
CW	continuous wave.
DC	direct current.
DFG	difference-frequency generation.
EM	electron microscopy.
EO	electro-optic.
FDTD	finite-difference time-domain.
FEL	Free-Electron Laser.
FN	Fowler-Nordheim.
FWHM	full width half maximum.
HDPE	high-density polyethylene.
LEEPS	low-energy electron point source.

NIR	near-infrared.
OAPM	off-axis parabolic mirror.
PPM	point-projection microscope.
PTFE	polytetrafluoroethylene.
RF	radio-frequency.
RMS	root mean square.
SEM	scanning electron microscope.
SFE	Schottky field emission.
TEM	transmission electron microscope.
THz	terahertz.
UEM	ultrafast electron microscopy.
UTEM	ultrafast transmission electron microscopy.

Chapter 1

Introduction

In recent years the advent of ultrafast electron microscopy (UEM), a technique that combines the high spatial resolution of electron microscopy (EM) with the temporal precision of ultrafast pulsed lasers, has opened new frontiers in capturing the transient states of matter at the atomic scale. This quest began with the development of the transmission electron microscope (TEM) by Ruska in 1932 [11], a tool that promised to harness the sub-angstrom wavelengths and robust interaction of electrons with matter. Dennis Gabor's subsequent proposition of electron holography in 1948 [12] further expanded our imaging capabilities, however, a lack of coherent electron sources initially hampered its application. Since then, significant strides in electron detection, beam manipulation, vacuum technology and the refinement of electromagnetic lenses have improved the resolution of these techniques towards the picometer scale [13].

Elsewhere, a revolution in ultrafast physics came in the 1980s with Strickland and Mourou's scheme for chirped pulse amplification of femtosecond laser pulses [14]. This innovation enabled the generation of short bursts of photo-electron, heralding the era of UEM [15] and permitting the visualization of dynamical processes such as phase transitions in solids [16] and the determination of molecular structures and reaction pathways of transient Fe(CO)4 [17]. These techniques made use of integrating smaller bunch charges to gain information on evolving processes. Since then, electron pulse compression methods, designed to overcome the temporal broadening effects of Coulomb repulsion have continuously improved temporal resolution. The next revolution is poised to come from single-shot operation, where individual electron bunches are bright enough to form an image, bringing the aspiration of capturing ultrafast single-shot dynamic sequences with angstrom resolution tantalizingly close to reality. As we venture further into this uncharted territory, the quest for brighter electron sources, more refined temporal resolution, and innovative experimental techniques becomes crucial. These advancements promise to not only deepen our understanding of fundamental physical processes but also pave the way for novel materials and technologies, setting the stage for the next revolution in scientific discovery.

Though the arsenal of microscopy has expanded over the centuries, no singular technique has emerged for all purposes. When it comes to 3D characterisation of materials the options are relatively limited. For single crystalline samples, X-ray crystallography has

been able to determine structure with great accuracy [18]. However, for obtaining structural information from discrete entities or amorphous samples, such as nano-particles or viruses, commonly TEM or X-ray scattering are used, and both involve taking many exposures in many orientations and using computational techniques to reconstruct a 3D structure [19]. These techniques thus require a large amount of high energy electrons or X-ray photons to enter the sample and limit us to beam insensitive materials. An alternative approach, low-energy electron point source (LEEPS) microscopy stands out by offering lensless imaging, minimal beam damage, intrinsic 3D information obtained through electron holography, as well as hypersensitive characterization of B and E fields [20]. LEEPS operates by emitting electrons from a metallic nanotip close to the sample, projecting a magnified image of the sample onto a detector. Historically this method has been underutilized due its inability to reach resolutions below 10 Å, a fact that was attributed to the insufficient divergence of electron sources [21]. However, recent advancements in electron emission and vibration reduction have enabled resolutions as fine as 1.7 $\pm$ 0.6 Å [10]. With further developments, we can now envisage the advent of single-shot femtosecond point-projection microscopy.

With origins in the late 19th century, when the photo electric effect was first observed by J. J. Thomson [22] and famously explained by Einstein [23], electron guns have since passed through many iterations. Electron sources are typically categorized based on their emission mechanism, which includes thermionic emission, photoemission, and cold field

emission (CFE). Historically, many sources have relied on photocathodes, surfaces designed to emit individual electrons through photoemission—in combination with electron lenses to generate transversely coherent bunches, with coherence lengths typically shorter than the intermolecular distances being observed [24]. However in recent decades the use of CFE from metal nanotips has been favored for many applications, as the geometry of the source both serves to amplify the incident field through the lightning rod effect and to emit highly transversely coherent electrons bunches [4]. Tungsten nanotips illuminated with single cycle terahertz pulses have been shown to emit highly monochromatic electrons, with $\Delta E/E \approx 1/1000$, with energies of 3.5kV with and bunches approaching 10^6 electrons per bunch, [6] providing excellent sources for a LEEPS microscope.

This thesis describes the design of a novel point-projection ultrafast electron microscope as well as recent developments in THz driven electron CFE. Chapter 2 outlines the theoretical background, including principles of TEM and UEM, electron field emission, THz pulse generation, as well as important design considerations of the microscope. Chapters 3 and 4 present our experimental setup and CFE data generated using THz pulses from a laser-induced air-plasma. Chapter 5 describes improvements made to the collimation of the air-plasma source, resulting in a fourfold increase in field strength at the focus. Chapter 6 describes the design of the novel PPM microscope to be built in 2025. Finally, Chapter 7 summarizes the results of this thesis as well as further experiments to be performed.

Chapter 2

Theoretical Background

This chapter briefly introduces TEM, UEM as well as ultrafast phenomena. The working principles of electron holography and point-projection microscopy will be presented, as well as key factors needed to achieve high spatial and temporal resolution. The theory of electron emission from a nanotip is then introduced as well as the generation of THz pulses.

2.1 UTEM and Ultrafast Phenomena

The development of EM marked a revolution in our ability to see beyond the diffraction limit of optical microscopy, into the atomic fabric of matter. Ruska's development of TEM exploited the unique properties of electrons as probes of matter. These electrons interact with atomic nuclei and electron clouds through Coulomb forces, providing a detailed view of materials at the atomic level.

In TEM, an electron beam is passed through a thin specimen, with the transmitted electrons being collected at the imaging plane to form an image or diffraction pattern. The diffraction mode relies on the scattering of electrons by the specimen, while the imaging mode relies on the modulation of electron intensities after transmission to provide a direct visualization of its microscopic features. Historically, these techniques were limited to observing static samples, due to the continuous wave (CW) or slowly varying nature of the electron sources. Early time-resolved electron studies used excimer lasers with a wavelength of 193 nm and a pulse width of 15 ns, achieving electron bunches with temporal resolutions of about 15 ns to study photochemical reactions including the photodissociation of CS_2 to the monosulfide C=S [25]. However, this limitation largely persisted until the advent of ultrafast lasers, which enabled the creation of ultrashort electron pulses and meaningful time-resolved studies with ultrafast TEM (UTEM).

With temporal resolutions that can reach into the ps and fs regimes, UTEM allows for the direct visualization of physical processes crucial to our understanding of condensed matter. From the atomic movements involved in chemical reactions, to molecular vibrations and rotations occurring on the order of fs and ps [26], UTEM unveils the dynamics of material transformations on the atomic scale. These dynamics determine the macroscopic properties of materials through the interplay among charge, spin, orbital, and lattice-structural degrees of freedom. The interactions between phonons and charge carriers, for example, are integral to the electrical and thermal properties of materials and

influence a range of technologies, from photovoltaic devices to thermoelectric materials [27]. Understanding these carrier-phonon interactions is essential for explaining and harnessing phenomena such as superconductivity, charge-density waves and phase transitions.

Furthermore, the ability to coherently excite samples with fs laser pulses allows for the study of materials under non-equilibrium conditions. In such states, the interplay between different degrees of freedom can lead to a multitude of nearly degenerate ground states, each with its own unique set of properties. Mode-selective excitations, enabled by precise control over stimulation, have the potential to induce new states and phases with exotic behaviors.

In time-resolved TEM studies, an optical pulse disrupts the sample's equilibrium, followed by an electron pulse that probes the ensuing relaxation phase, in what is known as a pump-probe measurement. Adjusting the interval between these two pulses allows us to record the dynamical process as the sample returns to equilibrium. Fine-tuning this delay is typically done using mechanical translation stages, providing fs to ps time delay. Importantly, both the stimulation and observation phases must be considerably shorter than the natural timescale of the phenomena being examined to prevent the blurring of temporal details.

2.2 Electron Probes

Following sample excitation, probing can be conducted in two distinct experimental frameworks, with single bursts of electron pulses or through cumulative exposure over multiple cycles. In single-shot mode, the electron bunch is typically made up of 10^5 and 10^8

electrons to obtain a diffraction pattern or an image, respectively. In the stroboscopic mode, a large number of pump-probe events are integrated, until enough information is accumulated about the sample at the given time delay. This method may only be used on highly repeatable processes, in which the sample is guaranteed to return to the same state after each excitation. The stroboscopic mode can thus use electron bunches with as few as one electron, reducing or eliminating the effect of Coulomb repulsion within the bunch and improving temporal and spatial resolution [28]. Single-shot experiments, with their large bunch charges, meanwhile suffer from large collective repulsion known as space charge effects [29], often requiring complex beam compression to mitigate these effects. In practical applications, most measurements make use of the stroboscopic method using large bunches, as the electron count needed for single-shot acquisition varies greatly depending on the specific light-induced change being observed.

Ensuring the spatial and temporal coherence of electron probes is key to unlocking precise visualizations of evolving processes. Critical to UTEM is the timing resolution of the electron pulse itself, determined by the initial energy distribution as well as temporal broadening due to space charge as it propagates towards the sample. Achieving sub-ps time resolutions with large bunch sizes remained elusive until 2003, when Siwick *et al.* demonstrated ultrafast laser-induced solid-liquid phase transition of aluminum using bunches containing 6000 electrons accelerated to 30 keV with 600 fs resolution [16]. Here, the time resolution was achieved by simulation-informed design of the photo-emission gun and choice of operating parameters.

These simulations further suggested the presence of a linear velocity chirp on the electron pulse, and the possibility of using pulse compression to improve timing resolution [30].

The linear velocity chirp arises as higher energy electrons advance to the pulse's front while those with lower energy start to lag. Additionally, space charge pushes electrons at the pulse's leading edge ahead, while those at the rear are propelled backward. This creates longitudinal spreading of the electron pulse and a radial expansion, causing the initially pancake-shaped bunch at the photocathode to evolve into an ellipsoid under space charge forces. Techniques using radio-frequency cavities were then proposed as a method to re-compress the beam in both transverse and longitudinal directions [31]. This technique has since allowed for the development of single-shot fs electron diffraction, with bunch sizes exceeding 10^6 and time resolutions below 100fs [32].

As for single-shot direct imaging, the requirement for bunch charges in excess of 10^7 historically precluded its use. This minimum electron flux is given by the need to distinguish sample features having 50% contrast with five distinguishable gray levels. According to the Rose criterion [33], which describes the number of particles needed to maintain shot noise below 10% and achieve a signal-to-noise ratio of 5, 100 or more electrons are needed per spatial resolution unit d. For a desired resolution of 3nm and an image size of 1 um^2, we find 10^7 electrons or 10 electrons per nm^2. This analysis importantly does not take space charge effects into account, which would significantly worsen the resolution value given above.

The first example of single-shot UTEM came in 2006, with LaGrange *et al.* setting a

precedent using 200 kV electron pulses with bunch charges exceeding 10^7 electrons, achieving temporal and spatial resolution of 30 ns and 20nm respectively [34]. These relatively modest resolutions were due to a lack of techniques employed to counteract space charge. In 2014, researchers at UCLA achieved single-shot MeV TEM with 10-nm–10-ps resolution and bunch charges of 10^7 [35]. Here, the use of relativistic energies effectively bypasses the need for compression, as higher energy electrons possess both a smaller de Broglie wavelength, increasing spatial resolution, as well as shorter transit time, reducing temporal broadening. However, higher energy electrons present an elevated risk of sample damage from radiation effects, rendering them unsuitable for sensitive materials like biological specimens. Additionally, such energies require electron optics with significantly more powerful magnetic fields to focus the beam accurately, increasing the system's complexity and cost

2.3 Point-Projection Microscopy

While the above examples were based on traditional TEM, alternatives relying on projection imaging has also shown promise for ultrafast applications. Such techniques have previously achieved 20-nm spatial resolution and a 25-fs time resolution with sub-keV single electron probes [36]. Point-projection microscopy (PPM) employs electron gun-sample distances orders of magnitude shorter than traditional TEM's, serving to reduce transit times and temporal broadening. Additionally, the low bunch charges and

electron energies have marked PPM as a method suitable for beam sensitive materials.

First demonstrated in 1939 by Morton and Ramberg [37], PPM entails placing a diverging point-like electron source near a sample and projecting its shadow on a distant plane of the detector, as shown in Fig. 2.1. With atomically sharp metal nanotips serving as point-like field-emission sources of electrons, the magnification is given by: $M = D/d$, where D and d are the source-detector and source-sample distance, respectively.

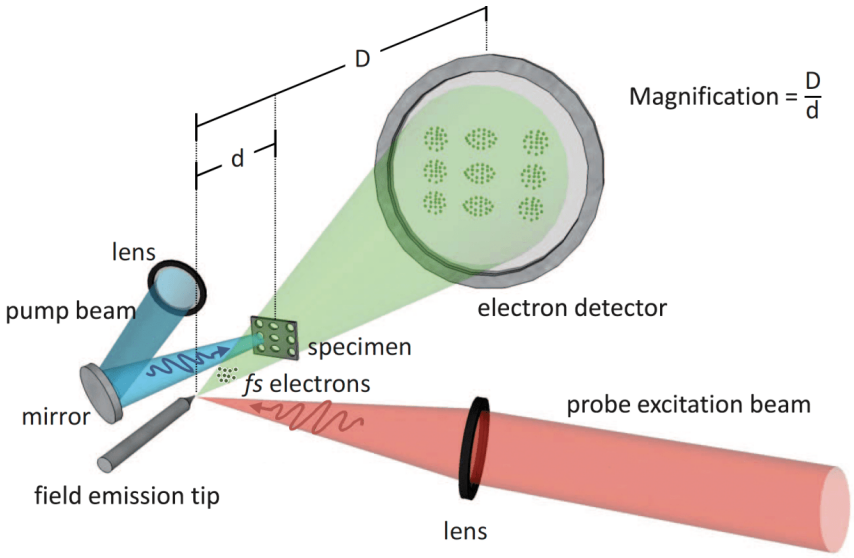

Figure 2.1: Schematic of femtosecond photoelectron point-projection microscope adapted from [1]. The pump beam excites the sample, while the probe excitation beam triggers the generation of an electron pulse via field emission. These electron packets illuminate the sample and are collected at the detector plane.

When considering electrons as rays, the projection gives a direct outline of the object, with the wave nature of electrons leading to interference fringes on the edges of the projection, as shown in Fig. 2.2. These fringes form what is known as an in-line hologram and can be

used to extract phase information about the wave packet at each plane of propagation. This phase provides information about local variations in B fields and electrostatic potential both within and surrounding the specimen, and differentiates PPM from most conventional TEM techniques. [20].

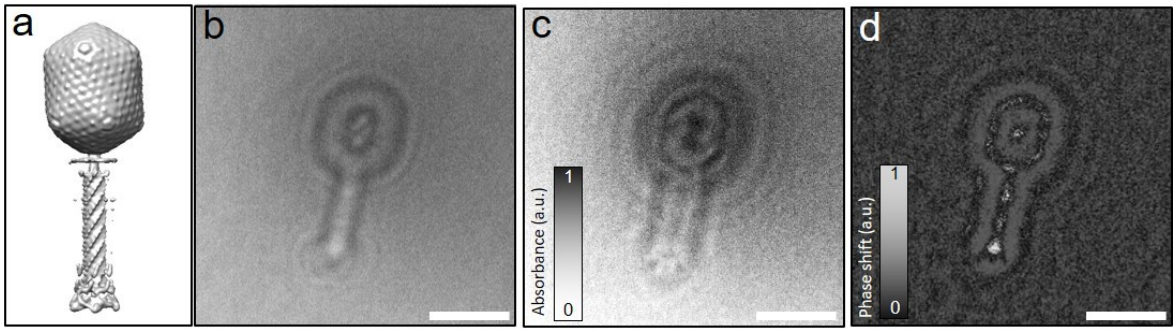

Figure 2.2: Image adapted from [2] illustrating low-energy in-line electron holographic images of vitreous ice-embedded biomolecules. Panel (a) diagram of the known structure of the bacteriophage T4 virus, (b) shows the recorded hologram, (c) and (d) are reconstructions that show the contrast from amplitude and phase respectively. All scale bars are 100 nm.

As a lens-less approach, PPM offers a significant advantage in cost and ease of operation. Furthermore, by removing the need for lenses, PPM is theoretically free of aberrations caused by focusing imperfections that can distort the image. In practice however, the finite width of the source, as well as mechanical vibrations and stray fields can significantly degrade the quality of the image. The combination of these various factors can be calculated and together used to define an effective or virtual source size [38].

To ensure the appearance of fringes, a highly coherent source of electrons is needed as well as high mechanical stability. Spatial coherence is the degree of phase correlation along

the wave fronts, with true point source emitters being perfectly spatially coherent. Here again, the energy bandwidth, ΔE, of the electrons is critical, as an independent interference pattern will appear for each electron energy, leading to attenuation of higher order fringes and blurring.

Though the proximity of the sample from the source has advantages, as mentioned previously, it complicates pump-probe experiments. For the typically small values of d desired to achieve large magnification, the light pulse used for field-emission will also impact the sample. This, along with mechanical vibrations threatening to crash the nanotip into the sample, ultimately limit d and the instrument magnification [1].

Another consideration for achieving high spatial resolution is the divergence angle, α, of the beam as it relates to numerical aperture (NA). The smallest feature that can be resolved by a given optical system, R, is related to its numerical aperture by [39]:

$$R = \frac{\lambda}{2NA} = \frac{\lambda}{2sin(\alpha)} \tag{2.1}$$

This sets a limit for resolution that is independent of beam coherence. To generate an image with high-resolution the electron source must emit a wide beam [21]. For example, with an electron wavelength (λ) of 0.39 nm at 1 keV, dividing this by $2\sin(5°)$ yields a resolution (R) of 2.237 nm. However, if we use $2\sin(30°)$, the resolution improves significantly to 0.39 nm. This prompts a closer look at electron source engineering, where there have been many

recent improvements.

2.4 Light-Field Electron Emission

When selecting an electron source for UTEM and PPM, the main criterion is high transverse brightness, given by [40]:

$$B_n = \frac{I_p}{4\pi^2 \epsilon_n^2} \tag{2.2}$$

where $I_p = \frac{Q}{\sqrt{2\pi}\sigma_t}$ is the peak current, Q is the total charge, σ_t is the pulse duration, and ϵ_n is the normalized emittance. The normalized emittance ϵ_n is a measure of the beam quality, given by the following equation [41]:

$$\epsilon_n = 2r_s \left(\frac{k_B T}{mc^2}\right)^{1/2}$$

where r_s is the beam radius, k_B is the Boltzmann constant, T is the temperature, m is the mass of the electron, and c is the speed of light. The emittance, along with the total charge and pulse duration will heavily influence the spatial resolution, the spatial coherence and the temporal resolution, respectively. This equation is only valid in the vicinity of the emitter, as space-charge forces will expand the bunch upon propagation. Notably, a large angle will reduce brightness, but as stated earlier it is critical to obtaining high resolution

images in PPM. For this reason, maintaining sufficient brightness for imaging with a large angle requires exceedingly many electrons. Other criteria of importance include electron energy bandwidth (ΔE) and width of emitting surface. A narrow ΔE improves brightness, as it reduces momentum spread and pulse duration at the sample. A smaller emitting surface improves spatial coherence, reducing blurring of details in the interference patterns that can occur with multiple point sources.

There are several types of electron emission processes commonly used in TEM which include thermionic emission, photoemission, cold field emission (CFE) and Schottky field emission (SFE). Each method aims to overcome the electrons' binding potential V(x), with the barrier height known as the binding energy E_b or the work function (ϕ) in the case of metals. In thermionic emission a cathode is heated, shifting the Fermi-Dirac electron distribution to include electrons with energies above the vacuum level, causing emission from the material. Photoemission occurs when a material absorbs one or multiple photons of sufficient energy, surpassing the work function and leading to electron emission into the vacuum. CFE involves applying a strong electric field to a nanotip, lowering the potential barrier and enabling efficient electron tunneling from the Fermi level. SFE uses a field-assisted thermionic emission from a cathode, where the applied DC electric field lowers the material's effective work function, facilitating thermionic emission at lower temperatures.

For ultrafast applications, thermionic and Schottky field emission are unsuitable as the time required for temperature stabilization precludes rapid modulation of the electron current

[42]. Instead, the adoption of CFE and photoemission triggered by ultrashort laser pulses has proven effective, enabling the generation of electron pulses with fs duration. Here, the distinction between CFE and photoemission is delineated by the Keldysh parameter (γ_K), defined by the ratio of tunneling time (t_{tun}) and the driving laser oscillation period (T) : $\gamma_K = t_{tun}/T$ [43]. Multiphoton photoemission emerges as the dominant mechanism for $\gamma_K >> 1$, and field emission for $\gamma_K << 1$. One can selectively transition from a multiphoton to a field-dominated process by increasing the driving laser's wavelength, keeping the field the same, thereby extending the laser's oscillation cycle.

Operating in the field emission regime is generally advantageous over photoemission, which is limited by the damage threshold of materials under photon-induced heating [44]. Additionally, photoemission requires an extra step to accelerate electrons after emission, while in CFE, the local field drives the electrons to tunnel and subsequently accelerates them. The tunnelling rate is given by the Fowler-Nordheim (FN) equation [45]:

$$J = \frac{aF_{loc}(t)^2}{F_\phi^2 \phi} e^{-vb\frac{F_\phi}{F_{loc}(t)}} \tag{2.3}$$

where a and b are the FN constants equal to 1.54×10^6 A eV/V^2 and 6.83×10^9 V eV$^{3/2}$/m respectively [46]. F_{loc} is the local electric field, and F_ϕ is defined as the field required to narrow the potential barrier to 0. This framework outlines two distinct regimes: one where $F_{loc} << F_\phi$, where emission is given by an exponential field dependence; and another where $F_{loc} >> F_\phi$, causing the exponential term to saturate and $J \propto F_{loc}^2$. Here, $v \approx 1 - \frac{F_{loc}}{F_\phi}$,

represents the influence of image charges, exponentially suppressing the emission for $F_{loc} < F_{\phi}$ [47].

Key to both emission techniques is the use of metallic nanotips with apex radii of 100nm or less as the target for ultrafast laser pulses. Before the introduction of nanotips for photoemission, flat photocathodes were used, setting the electron emission region equal to the laser's focal spot size on the cathode, approximately 20–30 μm [42]. Nanotip emitters, in contrast, significantly narrow the emission area down to the tip's apex, enhancing brightness. Nanotips also benefit from what is known as field enhancement, due to the lightning rod effect, which describes the redistribution of electric charges to cancel an electric field inside a conductor. This leads to a concentration of charge at points of high curvature and thus intensifying the external field at the tip apex, as shown in Fig. 2.3 [3].

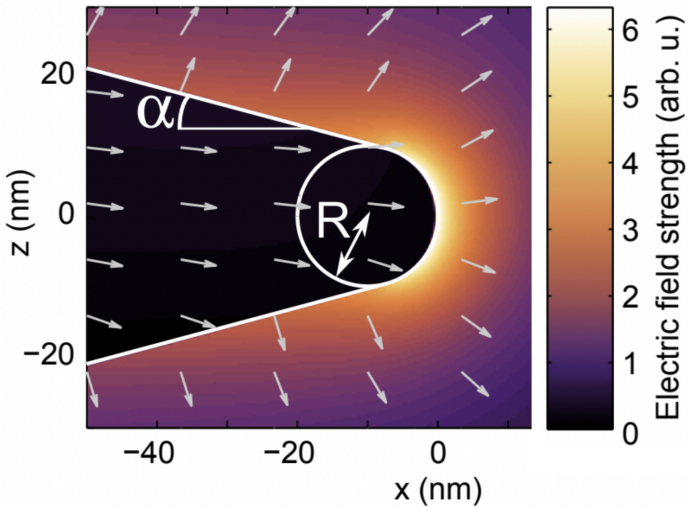

Figure 2.3: Image adapted from [3], showing electric field enhancement at the surface of a tungsten nanotip of radius 10 nm, under illumination of an 800 nm laser pulse propagating in the z direction, polarized along the x direction.

The factor by which the incident field (F_0) is enhanced is given by $\gamma = \frac{F_{loc}}{F_0}$. Importantly, γ scales as $\frac{\lambda}{R}$, where R is the tip radius and λ is the wavelength of the incident light [48].

Upon being ejected from the surface, electrons undergo acceleration and gain energy proportional to F_{loc}, which quickly diminishes to F_0 over a distance comparable to R, with $\gamma(x) = \gamma/(1 + 2x/R)$ for a hyperbolloid tip [5, 49]. Since the electrons depart this region in a timeframe significantly shorter than the period of the driving light, F_0 can be considered approximately constant during this interval. Consequently, the energy gained by the electrons is equivalent to the work done by F_0, approximately the product of the average electric force $\frac{1}{2}\gamma e F_0$ and the local field enhancement region, $\sim R$ [5]. This relationship however implies a large dependence on R, on the final electron energies that was not demonstrated experimentally. To explain these observations, Li *et al.* used the fact that γ, for a hemisphere-capped cylinder of length L and radius R in a static field, is proportional to $\frac{L}{R}$ [50]. This value can be further simplified to remove the length dependence, L, as retardation effects will limit the effective length of the emitter to $\lambda/2$ [51]. Plugging this into the earlier expression we find:

$$\Delta E \sim \frac{1}{4} e F_0 \lambda \tag{2.4}$$

Thus we have a direct relationship between electron energy and incident field as well as illuminating wavelength λ, that is independent of R.

The pioneering use of nanotips for electron emission was demonstrated with nanosecond

pulses in 2002 [52], followed by the generation of femtosecond electrons in 2006 [53]. These early demonstrations employed low power, high repetition rate, near-infrared (NIR) lasers, where the emission process was a mix of photo-emission and field emission with $\gamma_K \approx 0.1$. Subsequent advancements in the development of high-field THz generation saw the introduction of THz-driven CFE, marking a significant milestone.

THz light, with its long wavelengths (1 THz = 300 μm), benefits from several properties which bring the emission into deep sub-cycle cold field regime with $\gamma_K << 1$. THz pulses benefit from large field enhancements when coupled to metal nanostructures, as longer wavelengths enable the quasistatic approximation, where the electromagnetic field variation over the structure is minimal, and by matching the resonant frequencies of metal nanostructures [54]. The nonlinear field dependence of the emission leads to emission duration shorter than the THz half-cycle responsible for the emission.

Below, key results in THz-driven nanotips are showcased, starting with Herink *et al.*'s 2014 study, in which plasma-generated THz pulses, centered at 1 THz with peak fields of 10 kV/cm, were targeted a tungsten nanotip with a 10 nm radius. This produced 50 fs electron pulses, with electron energies of 120 eV aided with a -40 V bias, and yielding about 50 electrons per bunch [4]. Following this, in 2016 Sha Li and R.R. Jones achieved electron energies surpassing 5 keV using THz pulses of 450 kV/cm, with a central frequency of 0.15 THz, employing tungsten tips ranging from 10 nm to 1000 nm in radius [5]. They observed that electron energies were only marginally affected by the tip radius, with radii differing

by a factor of 40 producing a variation in ΔE of only a factor of 2. Although their setup could not measure bunch charge, projections based on the electron energies and FN theory suggest figures likely exceeding 10^6 electrons. Most recently, Matte *et al.* in 2022 achieved bunch charges of 10^6 electrons per pulse with peak THz fields of 298 kV/cm and a central frequency of 1.24 THz, reaching maximum energies of 3.5 keV [6]. This electron count surpasses previous CFE results by three orders of magnitude, inspiring this work and the development of a single-shot ultrafast PPM microscope.

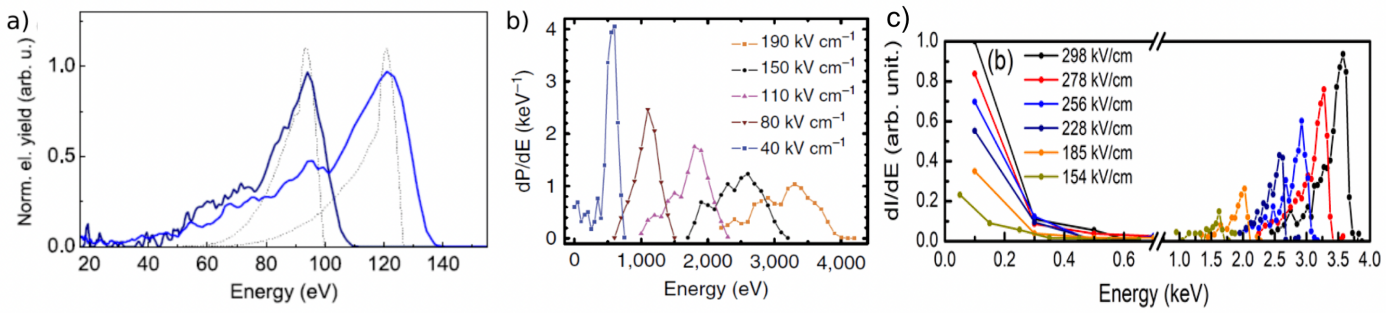

Figure 2.4: Electron energy spectra from THz cold field emission experiments adapted from (a) Herink *et al.* [4], (b) Li and Jones [5], (c) D. Matte *et al.* [6]. Dashed lines in (a)represent numerical simulation.

Interestingly, as is shown in Fig. 2.4. Herink *et al.*, operating in the low energy regime, found relatively wide peaks with $\frac{\Delta E}{E} \approx \frac{20eV}{90eV} = 0.22$, with distinct low energy tails present. The work of Li and Jones, meanwhile shows much broader energy peaks $\frac{\Delta E}{E} \approx \frac{1.5keV}{3keV} = 0.45$ and increasingly broad with higher energy, with no low energy tail present. Finally Matte *et al.* showed much sharper peaks with $\frac{\Delta E}{E} \approx \frac{0.5keV}{3.5keV} = 0.14$, but here there appears to be a

very pronounced low energy tail. This tail is made up of only energies below 0.3 keV, with the number of electrons in this range increasing nonlinearly with field strength.

Matte *et al.* presented a potential explanation for their spectra using known fluctuations in laser power of 2% RMS. Simulating for these shot-to-shot deviations in the laser intensity and subsequent fluctuations in THz field strength, they showed a broadening of the electron peak and the tail consistent with experimental observation. This further suggested that if one were to observe individual pulse spectra, they would be highly monochromatic as shown in Fig. 2.5, with predicted spectral purity of $\frac{\Delta E}{E} = 10^{-4}$.

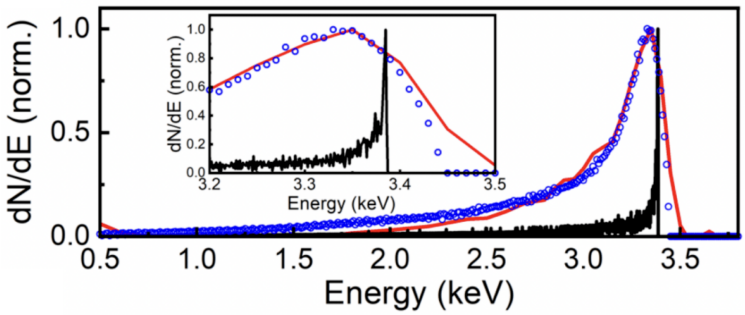

Figure 2.5: Figure adapted from D. Matte *et al.* [6], showing electron energy distribution (blue circles), with a simulation of the single-shot energy distribution (black line) given by FN tunneling theory and ballistic acceleration by F_{loc}, with an added 2% field strength fluctuation (red line). Inset: Magnified view of high-energy portion of the spectrum.

2.5 Terahertz Light Generation

Advancements in tabletop laser technology, notably in Ti:Sapphire near-infrared (NIR) lasers, have democratized access to high field THz pulses, a region of the electromagnetic

spectrum previously only accessible using large-scale, costly Free-Electron Lasers (FELs) that generate intense THz radiation [55]. The broad gain spectrum and capacity of ultrafast laser systems to deliver intense femtosecond pulses have propelled a wave of research into nonlinear optics and THz generation. Such systems are now capable of producing single-cycle THz transients containing high fields in the MV/cm, of approximately 1 picosecond duration, with frequencies ranging from 0.1 to 10 THz, opening new frontiers in ultrafast spectroscopy and pulsed electron sources.

Though there are many techniques to generate THz radiation, for the purpose of electron emission we desire a source which most efficiently produces pulses of large field strengths with a low central frequency. With this goal in mind, and when working within the typical constraints of tabletop lasers as sources of THz, there are three candidate techniques: optical rectification (OR), two-color plasma generation, and large aperture antennas. Both OR and air-plasma are non-linear processes which take advantage of the optical response of a media to an incident laser pulse to generate THz. A process is said to be non-linear when a material's polarization response to an incident field does not scale linearly with field strength. In a linear medium, the induced macroscopic polarization P is given by:

$$P(t) = \epsilon_0 \chi E(t) = \epsilon_0(\chi^1 E(t) + \chi^2 E(t)^2 + \chi^3 E(t)^3 + ...) \tag{2.5}$$

Where ϵ_0 is the permittivity of free space, χ is the linear electrical susceptibility, and E denotes the electric field. By expanding this relationship into a Taylor series we obtain the

right hand side of Eq. 2.4. Doing so gives us χ^2 and χ^3, tensors of the third and fourth rank, corresponding to the second and third-order nonlinear optical susceptibilities, respectively.

In the process of OR, an NIR pulse is incident on a material with a high χ^2, such as ZnTe, to efficiently generate terahertz (THz) radiation. When a material is subjected to a field with multiple frequency components, the E^2 term can lead to sum and difference-frequency generation (DFG), with OR being a process of subtraction in a special case of DFG where frequencies match (or nearly match). The time-varying nonlinear polarization $P(t)$ then serves as a source term of THz electric field, with $E_{\mathrm{THz}} \propto \frac{\partial^2 P^{(2)}}{\partial t^2}$ [56]. Depending on the material, it becomes crucial to match the group velocities of the THz and NIR pulses to ensure that the THz continually generated by the NIR pulse remains in phase with the THz concurrently propagating. For this reason, materials such as ZnTe which possesses similar group velocities for THz ($n_{1THz} = 3.17$) and NIR ($n_{800nm} = 3.13$)[57] are highly desirable.

Other factors are the efficiency of the difference frequency generation process and damage threshold of the material being used. The conversion efficiency depends on the effective nonlinear coefficient of the material (d_{eff}). LiNbO3, with a high $d_{eff} = 168pm/V$ and damage threshold approaching critical fluences of J/cm2 [58] proves an ideal candidate for OR. Unfortunately, LiNbO3's group indices for THz($n_{1THz} = 4.96$) and NIR($n_{800nm} = 2.25$) are poorly matched, a problem that historically hampered its use for OR.

Hebling *et al.* overcame this challenge by introducing the tilted pulse front technique [59]. Due to the slower propagation of THz compared to NIR in LiNbO3, a cone-shaped

THz wavefront emerges, exhibiting a characteristic emission angle of 62 ° relative to the NIR propagation direction. This angle can be calculated based on the refractive indices of the materials and the phase matching condition [60]:

$$\theta = \arccos\left(\frac{v_{g,\mathrm{NIR}}}{v_{p,\mathrm{THz}}}\right) = \arccos\left(\frac{2.25}{4.96}\right) \approx 62^{\circ} \tag{2.6}$$

where $v_{g,\mathrm{NIR}}$ is the group velocity of the NIR pulse and $v_{p,\mathrm{THz}}$ is the phase velocity of the THz wave. By crafting the crystal so its output face is cut at 62 degrees relative to the input, and by tilting the NIR pulse front to this angle, they ensured the THz and NIR pulses to maintain synchronization. This innovative approach led to a power conversion efficiency two orders of magnitude higher than the ZnTe sources [57], enabling the generation of peak THz electric fields exceeding 1 MV/cm, covering a bandwidth of 0.1-4 THz [61].

Not only is this method the most efficient source of THz generation, it is also behind the current record of CFE of 10^6 electrons per bunch. For this reason, though it is not the method used to produce the results presented here, it is mentioned as the benchmark with which we will compare our results. To produce the results of this thesis, the method of air-plasma generation was used. In plasma generation, an intense, ultrashort laser pulse and its second harmonic are focused into a medium, typically a gas, creating a plasma filament that, in turn, produces THz through a χ^3 process [62]. The emitted THz maintains a constant emission angle (α), leading to a ring-shaped pattern akin to a Laguerre-Gauss or Bessel beam, shown in Fig. 2.6. Though originally described by a four-wave mixing of the two

frequencies [63], this did not account for changes in plasma length or polarization between fundamental and second harmonic.

Kim *et al.* then proposed the two-step photocurrent model, in which the focused beams ionize electrons in a gas to form a localized plasma filament, where free electrons coherently oscillate to generate THz [64]. Further model refinements included variations in filament length [65] and input polarizations [66], aligning with the experimental observations. The focused laser and its second harmonic can be written as the sum of two Gaussian pulses:

$$E_L(t) = E_1 \cos(\omega t) \exp\left(-\frac{t^2}{\tau^2}\right) + E_2 \cos(2\omega t + \phi_2) \exp\left(-\frac{2(t - \frac{\phi_2}{\omega})^2}{\tau^2}\right) \tag{2.7}$$

Here, t is time, w angular frequency of the fundamental and τ is the pulse duration. ϕ_2 indicates the phase difference between the fundamental and harmonic, while E_1 and E_2 denote the E field amplitude of the fundamental and harmonic, respectively. As the pulse travels, it encounters N_0 molecules, with $N_e(t)$ representing the time-varying count of ionized molecules, with ionization rate given by $\dot{N}_e(t) = W_{st}(t)[N_0 - N_e(t)]$. Here $W_{st}(t)$ is the static tunneling ionization rate. Post-ionization, an electron's trajectory is determined by the Coulomb force resulting from the two-color laser electric field, generating a current density $J_e(t)$ given by:

$$J_e(t) = \frac{e^2}{m_e} \int_{-\infty}^{t} E(t) N_e(t)\, dt \tag{2.8}$$

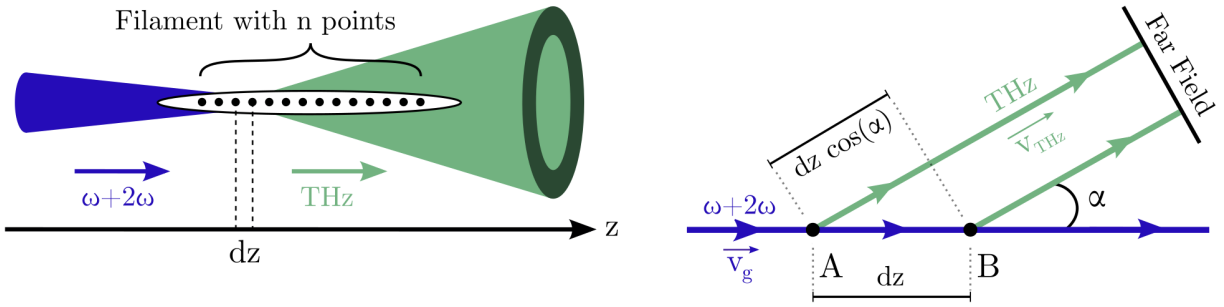

Figure 2.6: (a) Schematic of air-plasma THz field generation. An 800nm pulse and its second harmonic are focused creating a plasma filament from which a THz is emitted in a ring shape. (b) The plasma filament represented as an array of point sources each emitting at angle α, interfering with each other in the far-field. Fig. courtesy of G. Beaufort.

The photo-current is then the source of an electromagnetic potential $A(t) \propto J_e(t)$, with the generated THz being proportional to the time derivative of the potential $E_{THz} \propto \dot{A} \propto \dot{J}_e$. This analysis considers a single source point to be the origin of the emission. For plasma of finite length, it is possible to consider a linear array of point sources. By making the sources emit at an angle α and interfere in the far-field we obtain the ring-shaped emission profile.

The emission characteristics of the plasma can be optimized to maximize THz pulse energy. Increasing the number of free carriers that generate the THz currents can be achieved by utilizing gases with lower ionization potentials, such as argon or krypton [67]. Moreover, longer laser wavelengths result in higher THz pulse energy because the lower frequency of these wavelengths gives electrons more time to accelerate under the laser's electric field each cycle, leading to a quadratic increase in the ponderomotive force and enhanced THz generation [68]. Lengthening the filament further results in a greater number of ionized

electrons available for THz generation, increasing the power of the emitted THz [69].

However, employing longer filaments presents several challenges. Firstly, as we move along the focus the phase between the fundamental and its harmonic changes, as the two waves have different group velocities, with $L_{\Delta\phi=\pi} = 4\text{cm}$ observed in air.

Another issue lies in focusing the emitted THz, typically done using a lens or, as in our setup, an off-axis parabolic mirror (OAPM), which, although it minimizes chromatic dispersion from the broadband THz pulse, is designed to image only a single point in the filament. This configuration means that while the central point is imaged correctly, the rest suffer from imaging aberrations. Consequently, many researchers opt for filament lengths below 0.5 cm for better control over the output, accepting lower field strengths. For CFE, however, where field strength is critical, we forego this recommendation and maximize field strength by using a filament of 5 cm, forming the foundation of our experimental approach.

Chapter 3

Experimental Methods

In this chapter, we will describe the methods used for the emission and detection of electrons from tungsten nanotips. As this setup has been extensively described previously, we will focus only on the novel and most crucial aspects of the setup, namely THz generation via two color air-plasma, THz field characterisation, electron emission and detection. Further information about nanotip fabrication through electrochemical etching, tip annealing, field emission reshaping can be found in [70]. Information about the vacuum system used, including the vacuum chamber, pumping and vacuum gauge, as well as electronics and further detail on EO sampling and signal processing can be found in [8].

3.1 THz Field Generation and Detection

3.1.1 Two-Colour Air-Plasma THz Generation

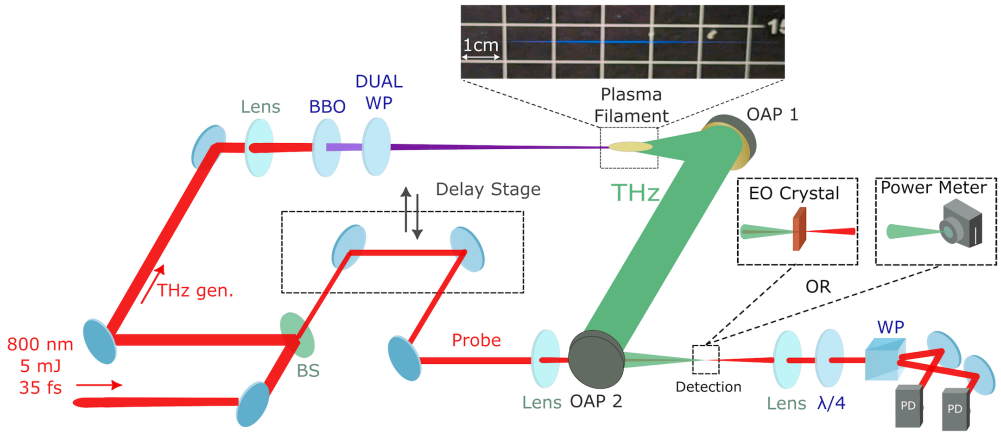

Figure 3.1: THz generation and detection diagram. The output of a Ti:Sapphire laser is separated into THz generation and detection lines. The NIR beam is focused, transmitted through a BBO crystal for 2nd harmonic generation, and a half-wave plate to align the two harmonics. A plasma filament is formed, generating THz which is collimated and focused on a power meter or co-incident on an EO crystal with probe NIR beam for balanced detection.

As shown in Fig. 3.1, a coherent Legend Elite Duo HE+ titanium-sapphire laser, emitting 35 fs pulses at 5mJ energy and 800nm center wavelength at a 1kHz rep rate, has its beam divided by a beam-splitter: 10% enters a delay line as a probe, and 90% for THz generation. This main portion is focused by a 50 cm lens to generate the plasma filament. A second harmonic at 400nm is generated using a 100 μm-thick Beta-Barium-Borate (BBO) crystal, cut at 29.3°, through type I second harmonic generation. The fundamental wave, initially horizontally polarized, aligns vertically with the second harmonic's vertical polarization,

achieved by rotating the fundamental wave's polarization by 90° using a zero-order half-wave plate, without affecting the 2ω polarization due to the plate's wavelength-dependent functionality. This ensures both beams share vertical polarization at the filament.

At the laser focus, air is ionized leading to the creation of a plasma filament exceeding 5 cm in length, as depicted in Fig. 3.1. This can be further extended by employing a longer focal length lens or utilizing more powerful pulses. The filament then emits an angled THz beam, which is collimated by a 4-inch off-axis parabolic mirror (OAPM), with a central hole for most of the residual laser beam and other plasma-emitted radiation to pass through to prevent damaging subsequent optics. The THz wave's donut-shaped emission profile allows it to bypass this hole unaffected. However, some plasma radiation still gets reflected by the mirror, which is then filtered out using a silicon wafer. The THz is then focused by a 3-inch OAPM and can be incident on either a power meter, EO crystal or tungsten nanotip for electron emission. A central hole through the focusing OAPM allows a probe NIR beam to pass through for EO sampling.

3.1.2 THz Detection

To detect and optimize our THz we employed several techniques including: direct beam visualization using a IRXCAM INO384 microbolometer array THz camera, pyroelectric power measurements using the Gentec-EO THZ4B-V-SCQW meter, and finally electro-optic (EO) sampling to get the THz waveform and frequency spectrum.

EO sampling takes advantage of the Pockels effect in a crystal, a χ^2 nonlinear effect, in which an applied electric field induces birefringence, resulting in different indices of refraction for different polarization directions. We are then able to detect THz by sending a linearly polarized NIR probe into the crystal and measuring the change in its ellipticity. After transmission, the NIR pulse passes through a $\frac{\lambda}{4}$ waveplate and becomes circularly polarized. This circularly polarized beam is then separated into two beams of vertical (I_A) and horizontal (I_B) polarization by a Wollaston polarizer, and are detected by two photodiodes. A schematic is shown below in Fig. 3.2.

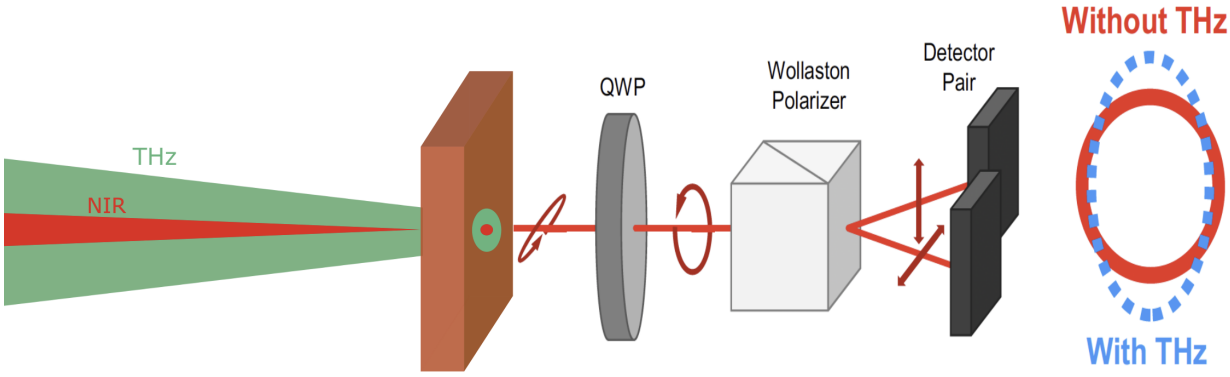

Figure 3.2: Schematic of EO sampling THz detection adapted from ref. [7]. THz and NIR probe beams are focused on an electro-optic crystal, resulting in birefringence and ellipticity of the transmitted NIR probe. The probe is then sent through a $\frac{\lambda}{4}$ waveplate and separated into polarization components by a Wollaston polarizer, with the change in polarization detected as an power unbalancing across two photodiodes.

Importantly both the THz and the probe beams are focused onto the crystal, with the spot size of the probe much smaller than that of the THz. This is to ensure we probe only the region of highest electric field, making the measurement less sensitive to noise. The

two pulses must also overlap temporally, which is achieved using translation stages, where moving the 35fs probe pulse along the ps-long THz pulse allows us to obtain information about a small portion of the THz waveform.

Mathematically, the phase retardation (ϕ) is linearly proportional to the instantaneous THz field E_{THz} and is given by [71]:

$$\phi = \frac{2\pi n_0^3 r_{14} E_{THz} L T_{Fr}}{\lambda}. \tag{3.1}$$

Here, n_0 and λ denote the refractive index and wavelength of NIR, r_{14} the crystal's electro-optic coefficient, L the interaction length, T_{Fr} the transmission coefficient [72].

The presence or absence of THz on the crystal will cause the detected I_A and I_B to be modulated. In the low field regime, the phase shift (ϕ) is approximately $sin(\phi) \approx \phi$ and is given by:

$$sin(\phi) \approx \phi = \frac{I_A - I_B}{I_A + I_B} = \frac{\Delta I}{I_0} \tag{3.2}$$

3.2 Electron Field Emission and Detection

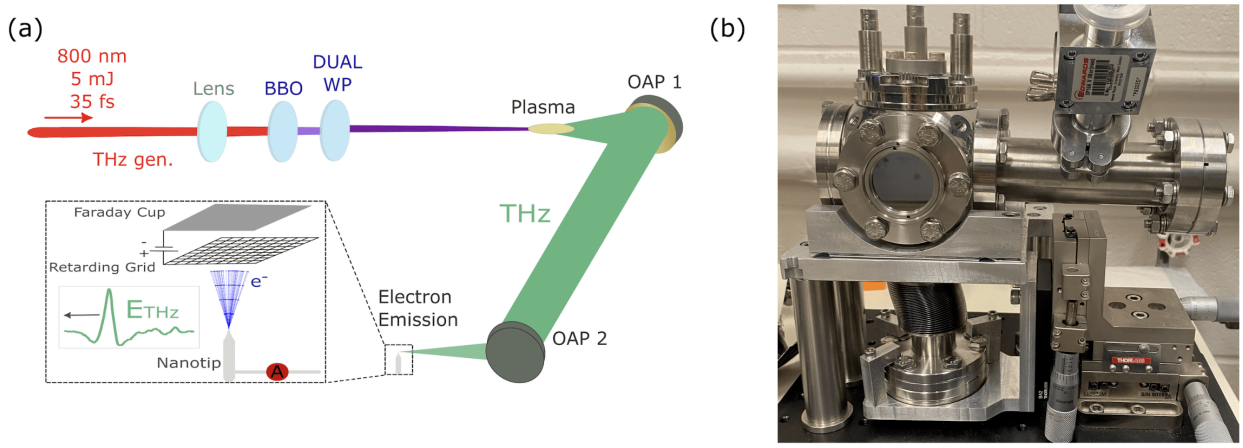

Figure 3.3: (a) Diagram of electron emission setup. (b) Side view of vacuum chamber with Faraday cup in place, showing silicon window, chamber mount and 3-axis translation stage connected to nanotip via bellows.

The tungsten nanotip is housed inside a spherical cube vacuum chamber with six 2.75 inch ports, shown in Fig. 3.3 (b), held at 10^{-6} Torr. Three of the four side ports serve as optical access, with one non-THz transmissive glass for visual access and a Z-cut quartz window allowing for THz coupling or coupling of a diode alignment laser, while a 3 mm thick high resistivity float-zone silicon window is used for THz coupling to the nanotip. The back port contains electrical feed-through to the nanotip and connects to the vacuum pump. The bottom port is attached to a bellows and manipulation stage used to scan the tip in X-Y-Z directions inside the chamber. Finally, the top port holds a Faraday cup detector which we use to characterize our electron energy spectra.

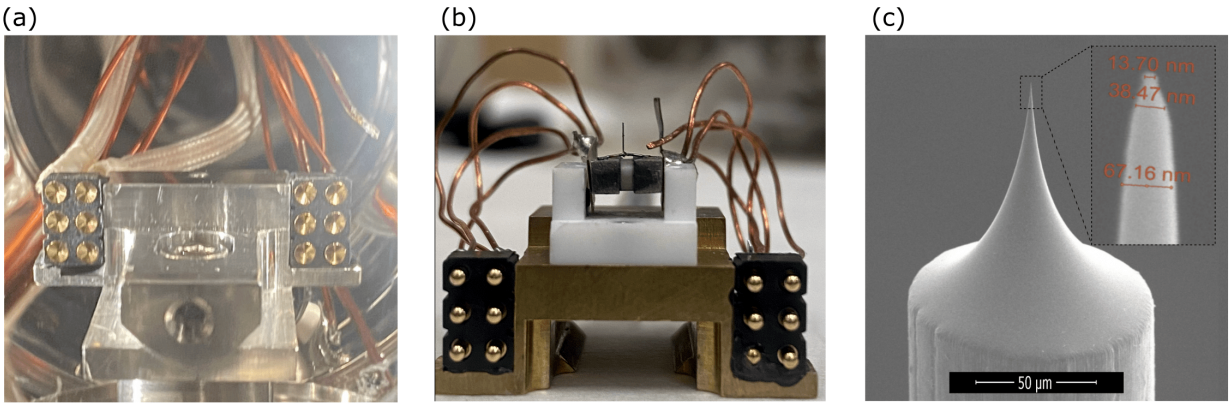

Figure 3.4: (a) Nanotip carrier rail with female electrical connections. (b) Nanotip and carrier which slides onto the rail from (a), with male push-pin connectors linking nanotip on either side to electrical feed-throughs. (c) SEM image of tungsten nanotip with inset showing zoomed-in apex with given tip diameter of 13.7nm.

As is shown in Fig. 3.4 (b), the tungsten nanotip is mounted between two copper plates on a electrically isolated U-shaped Macor base. Two 6-pin plastic push-connect electrical male connectors are glued on each side of the carrier using ultrahigh vacuum epoxy. The copper plates on either side of the tip are connected by 4 copper wires to the push-pin electrical connections, with each rated at 2 Amps. This is to allow for currents of up to 3 Amps to pass in parallel for tip heating during the annealing process and to add redundancy in case a connection is broken.

The nanotips are produced via electrochemical etching using the method described in [70], and reliably produced tips with apex radii of 10-20nm, with an example scanning electron microscope (SEM) image of a tip produced using this method shown in Fig. 3.4 (c). This image, shows a nanotip directly after manufacturing, which will undergo several changes

through the emission process. Firstly, during the annealing, a procedure of heating that is performed upon reaching vacuum to remove any absorbents from the surface of the tip, it is believed the radius and shape change significantly [70]. Secondly, the shape is known to change with exposure to THz pulses, with before and after SEM images of exposed nanotips showing significant alterations [8]. This is further proven in our emission experiments, which saw the detected current nearly halving over time, likely due to reshaping of the nanotip. For this reason our radius estimates contain significant uncertainty.

To measure the emitted electron current we use two methods, as shown in Fig. 3.3. Firstly, a Kimball Physics FC-73 Faraday cup detector, with a 5 mm diameter aperture, is placed roughly 2cm above the nanotip. The collection angle Θ, is then approximately 7 degrees, with only electrons emitted within this angle detected. Furthermore if the tip is not directly underneath the cup or if it is angled relative to the normal this will further reduce the collection efficiency. Other factors that will lower efficiency are space charge and stray fields, with both causing deviations in the electrons trajectories.

The Faraday cup is made up of 3 grids: the suppression, retarding, and ground grids. To decelerate electrons, a variable negative voltage ranging from 0 to 5 kV is applied to the retarding grid through a Moku voltage source amplified using Trek High Voltage Amplifier. This setup allows for the energy spectrum analysis of the electron beam by capturing only electrons with energy surpassing the applied retarding potential at the Faraday cup anode. By varying the bias voltage and observing changes in the detection current we can obtain an

electron energy spectrum. Moreover, applying a low bias voltage of -20 V to the suppression grid helps in reducing the detection of secondary and scattered electrons, thereby ensuring the accuracy of primary electron measurements.

The second method of current detection is via an electrical connection at the base. By removing the connection to one side of the tip, thus creating an open circuit, and illuminating the nanotip we can measure the replenishing current going toward the tip. This, unlike the Faraday cup measurement is not dependent on detector coupling efficiency and represents the entire tunneling current. The output of the Faraday cup anode or the base wire is connected to a Keithley 6517B electrometer, which records accumulation of charge over multiple electron pulses and returns a current measurement. Both currents can be measured simultaneously to determine the coupling efficiency as a function of THz field strength. A positive or negative bias voltage can also be applied to the tip instead of measuring the total electron emission current.

Chapter 4

Results

This chapter presents the results of our investigations into THz detection and electron emission. It begins with the estimation of THz field strength and beam profiling, followed by detailed measurements of THz emission angles. The chapter then examines electron emission results, including spatial and energy distributions, and concludes with a comparison of these results with EO sampling data to validate our field strength estimates.

4.1 THz Detection Results

4.1.1 Estimating THz Field Strength

We began by using a pyroelectric power meter and a microbolometer array camera located at the focus to optimize our alignment and image the beam profile. Images of the beam

at various positions in the propagation direction are shown in Fig. 4.1. From Fig. 4.1 (b) showing the beam profile at the focus we extract the following full width half maxes (FWHM): $\sigma_x = 380\mu m$, $\sigma_y = 345\mu m$. As we can see from Fig. 4.1 (c), for a distance of 16mm after the focus the beam displays the expected doughnut shape.

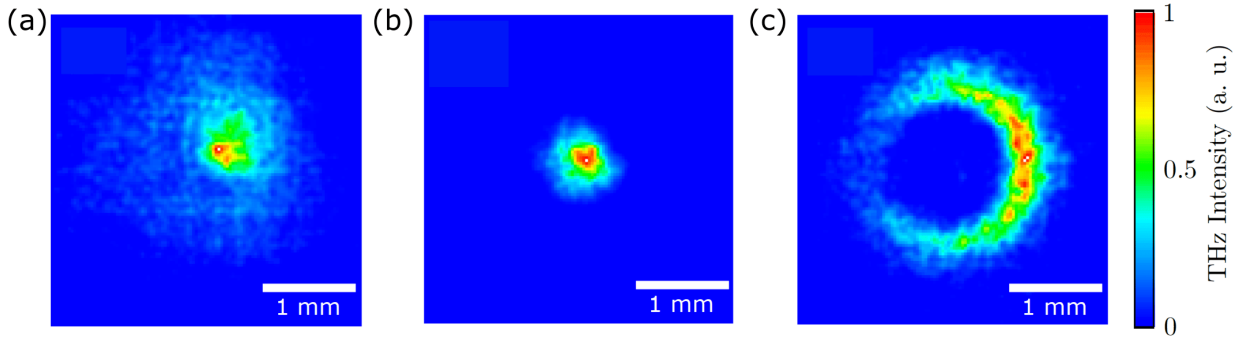

Figure 4.1: THz beam profiles measured with the INO camera at different Z positions, with intensity normalized relative to each image's brightest value. (a), (b) and (c) taken at -18mm, 0, 16mm from the focus respectively.

As for THz power, we detected 186μW, inferring the corresponding pulse energy U_p of 186 nJ, as measured by Gentec pyroelectric detector model THZ5B-VANTA. This method importantly does not offer any time resolution or field strength information, instead integrating all incoming beams. For a wide detector surface area, a poorly focused beam will result in the same power as a highly focused one. Furthermore if our THz beam is composed of several pulses being generated and arriving at different times, as we suspect it may be, a power measurement would not be able to distinguish them.

We then performed EO sampling to obtain a wavetrace of our THz pulse. Doing so

and optimizing we obtain the trace shown in Fig. 4.2 (b), which is shown beside a similar pulse in (a), that was produced by the tilted pulse front method and used to emit 10^6 electrons by Matte *et al.* As we can see when comparing our spectrum to that of Matte, the spectrum produced via OR is shifted slightly towards lower frequencies when compared to that generated via air-plasma, with central frequencies of 1.24 and 1.46 THz, respectively.

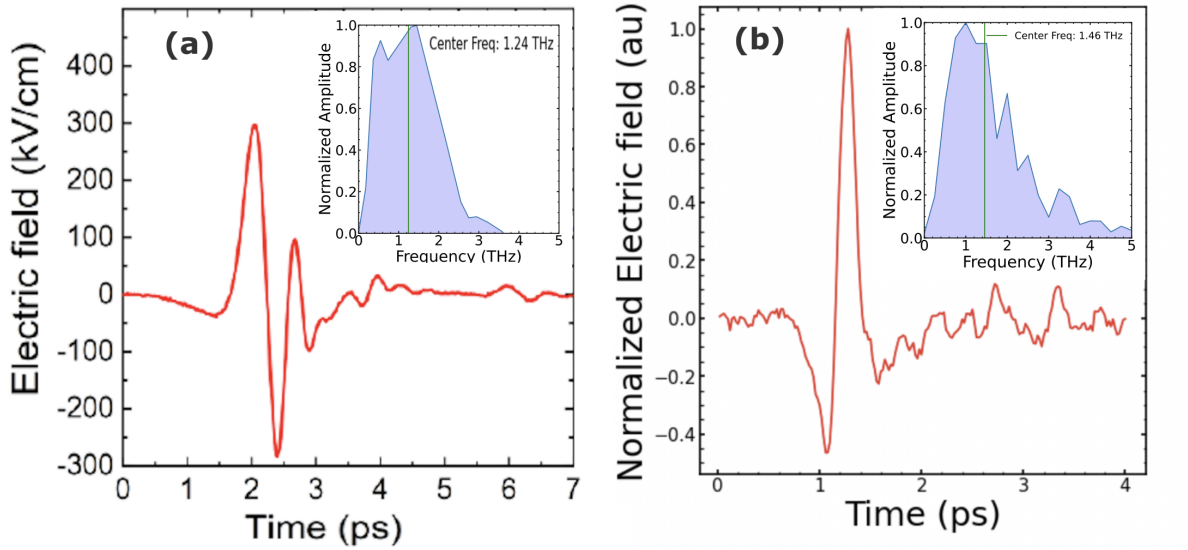

Figure 4.2: THz waveform and spectra for (a) THz generated using tilted pulse front technique which yielded 10^6 electrons in same setup as current experiment, adapted from [8], and (b) from air-plasma generation used in current experiment.

From another wave-trace, obtained using Air-Biased Coherent Detection (ABCD), we can normalize and square the field to get a time integral. The ABCD technique offers better timing resolution compared to EO sampling as it directly measures the electric field of the THz pulse without convolution with the phase matching response of the EO crystal. ABCD uses a setup where the THz electric field is detected through the nonlinear interaction of the

probe beam, the THz beam, and a bias electric field in air. A laser-synchronized alternating bias field applied between two electrodes generates a second harmonic signal proportional to the THz electric field strength. This coherent detection enhances the signal-to-noise ratio and provides a broad detection bandwidth, capturing the entire THz waveform with high temporal resolution [73].

From our ABCD wavetrace we obtain: $\int s^2(t)\,dt = 0.09ps$, giving us a preliminary field strength estimate, using the Poynting flux approach and our beam profile, pulse power, and pulse duration. This equation is given by [74]:

$$E_0 = \sqrt{\frac{ln(16)}{c\epsilon_0\pi}\frac{1}{\sigma_x\sigma_y}\frac{U_p}{\int s^2(t)\ dt}} \tag{4.1}$$

Plugging in our values of $\int s^2(t)\,dt$ =0.09 ps, U_p of 186 nJ, $\sigma_x = 380\mu m$, $\sigma_y = 345\mu m$, we find a peak field of $\approx$ 700kV/cm. This field is 2.5 times larger that what was used in study by Matte et al, and would be expected to yield approximately 10 times their electron bunch charge of 10^6 with peak energies exceeding 6 keV, thus motivating us to perform the experiment presented here.

Fig. 4.3 (a) shows the time-domain measurements of the THz electric fields as a function of the EO crystal's position along the propagation axis Z. The corresponding Fourier transforms are depicted in Fig. 4.3 (b). Interestingly, when scanning the EO crystal position, to map the field as a function of Z, we noticed something unusual. As the

probe and THz beam share the same path from the center of the OAPM to the crystal, it is presumed that the relative timing of their pulse trains should not change from moving the crystal in Z. This is not what was observed, however. Instead, when moving the crystal the signal disappeared and could only be found by changing the stage delay, thus adding a relative time difference between THz and probe pulses. Importantly, this suggests that several pulses are arriving staggered in time due either to different emission times in the plasma or difference in path length traveled by each point-emitter in the plasma filament. This is further explored in Chapter 5.

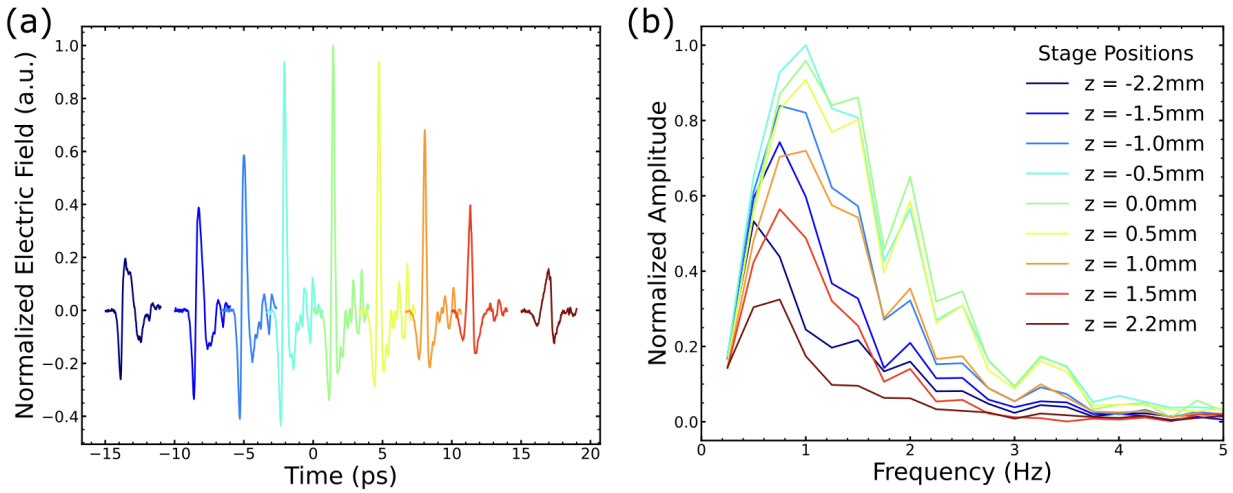

Figure 4.3: (a) Normalized time domain traces of the electric field as measured for different EO crystal positions along the propagation axis. (b) Normalized Fourier Transform of the time domain traces from (a).

This could also be a significant source of noise, with the crystal capturing several time-delayed pulses at once. It also importantly indicates that our field strength is highly overestimated, as mentioned previously, using a power meter cannot distinguish between a

single large pulse or several smaller ones arriving staggered in time. As others in the field have historically used Eq. 4.1 to obtain their high field estimates, this may point to a systematic overestimation occurring across the field. For this reason we will seek another method of field strength characterisation, using the electron emission data.

4.1.2 Measuring THz Emission Angle

As mentioned previously, the plasma source emits THz in a ring-like pattern with a characteristic emission angle Φ. We performed the following measurement to characterize the emission angle of our THz source. As shown in Fig 4.4 (a), by placing two apertures of different radii r_1, r_2 after the plasma and measuring power at the output we can map the power as a function of their relative distances z_1, z_2 and extract the emission angle Φ for each region of the plasma filament. Mathematically, we have:

$$\Phi = tan^{-1}(\frac{r_1 - r_2}{z_2 - z_1}) \tag{4.2}$$

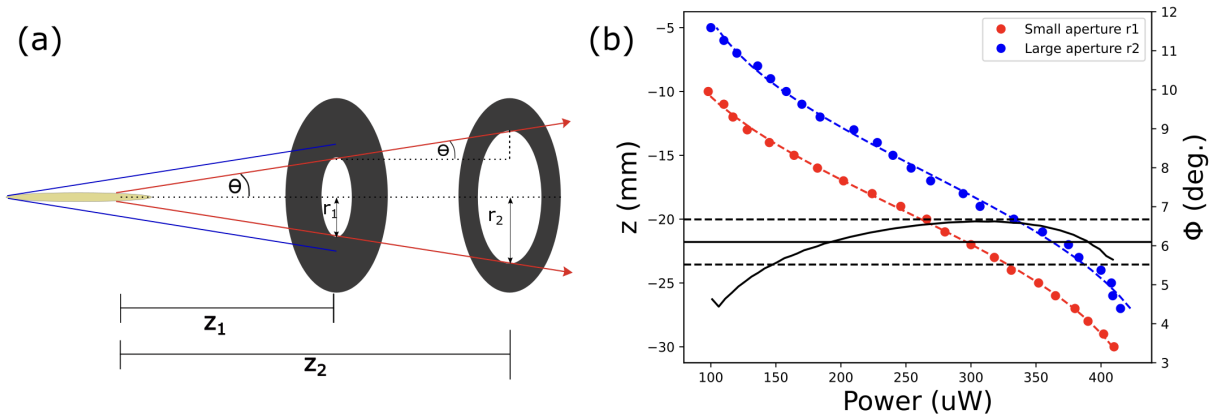

Figure 4.4: Characterisation of plasma filament emission angle, showing (a) schematic of measurement apparatus, (b) measured emission angle Φ as a function of detected THz power with an average angle of ≈ 6° shown as solid black line.

As we can see in Fig 4.4 (b), our measured emission angle is not constant along the filament, with both extremities having lower emission angles than the central region. We find an average emission angle of 6° with a maximum angle of 7°. Importantly we find a 7° beam will have a diameter of 0.99 inches at a distance of 4 inches from its origin, so a 1 inch-wide, 4-inch focal length OAPM will entirely capture the beam.

4.2 Electron Emission Results

To locate the THz focus with the nanotip we begin by shining a diode laser at the position of the THz focus. We find this point by placing a needle as in path of the THz beam in front of the THz camera until the detected pattern disappears. We then remove the camera and shine the diode laser from the opposite direction on the tip of the needle, giving us

an reference in X and Y. The same can be done in the Z direction so that we have two references points. By passing these alignment beams through the two clear vacuum ports give us starting point with which we can align our nanotip.

We then scan the tip in X and Y, while applying a pulsed negative bias to the tip, using the Moku waveform generator amplified by the high voltage amplifier. It is preferable to use a short excitation pulse, approximately 1 ns in length, as a large DC bias could cause rapid tip reshaping or even quench the emission altogether. The pulsed output can be monitored using an oscilloscope in combination with the laser trigger pulse to verify proper timing between the two. We begin with relatively large biases, beginning from -100V and increasing in -50V increments until emission is detected at the Faraday cup. Depending on the tip radii, the bias voltage can reach as high as -1kV before emission, see [70] for more information on biased emission. We then lower this voltage just below the emission point.

When no electrons are being emitted by the bias alone, we then scan the tip in X and Y, in the invisible path of the THz until electrons are once again being emitted, indicating the presence of THz. We then lower the voltage again and continue in this fashion until no voltage is required and THz alone is responsible for the emission. At this point we may switch to detecting the current at the base.

After coarsely scanning the tip in X-Y-Z and recording the base current for each step, we place the tip at the point of highest emission and proceed with THz optimisation. Parameters which can be repeatably altered include: the relative positions of the BBO crystal and

waveplate in Z, the rotation angle and face angle of the BBO crystal relative to the incoming beam, and finally the laser amplifier compression. After optimization was complete we proceeded to perform a fine scan of the nanotip in X, Y and Z.

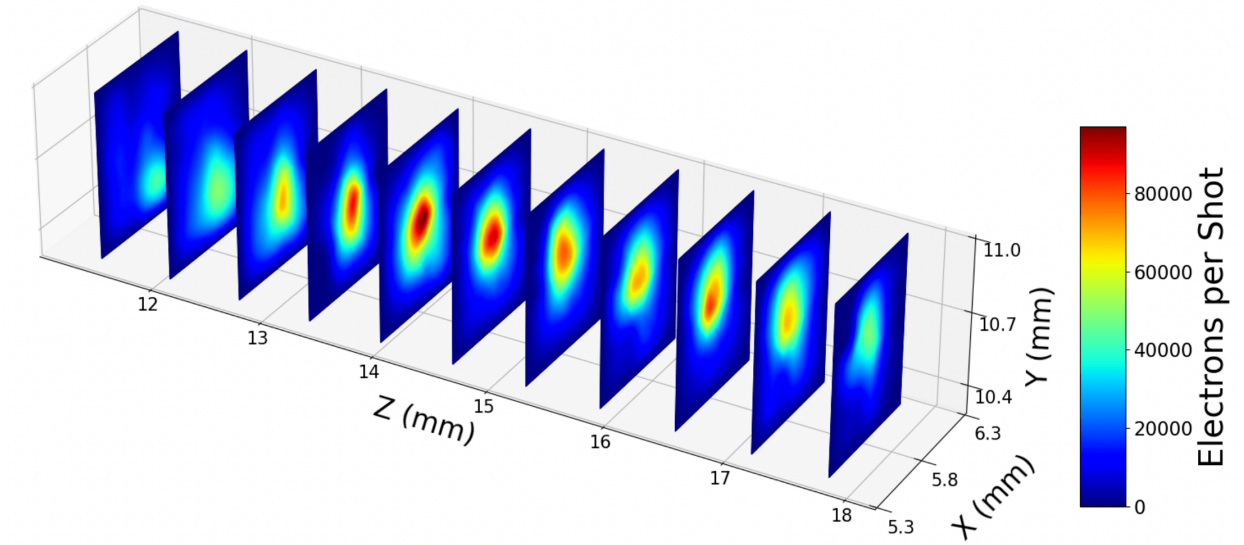

Figure 4.5: Interpolated electron emission cross sections for different values in Z.

The results of such a scan are shown in Fig. 4.5. As we can see at the central focus at $z = 13.97$ mm, we obtain 9.7x10^4 electrons per shot, though at other times during the experiment we saw as many as 2x10^5. In this figure the data is interpolated, with each Z-slice containing 20 grid values, for a step size of 0.127mm (0.005").

Looking at Fig. 4.5, it does not appear to exhibit the Gaussian profile expected from the focus of an air-plasma source [75]. To analyze this further, we determined the theoretical beam waist w_0 at $z = 13.97$ mm. This was done by taking the $1/2e^2$ value of the electron spatial distribution, as w_0 is an intensity measurement and $I \propto E^2$, and the electron count is

roughly $\propto E^2$ in FN theory, giving us $w_0 = 0.315$mm. This value was then used to estimate the expansion of the beam, using the Gaussian beam propagation equation [76]:

$$w(z) = w_0\sqrt{1 + \left(\frac{z}{z_R}\right)^2}, \quad z_R = \frac{\pi w_0^2}{\lambda} \tag{4.3}$$

where w_0 is the beam waist at the focus, and z_R is the Rayleigh length. Using our values of $\lambda = 225\,\mu$m (1.46 THz), we then calculate the expected beam waist ($w(z)$) at various distances from the focus. The resulting plot is shown in Fig. 4.6(a). The field strength at these points, plotted alongside the beam waists, was then estimated using the equation: E(z, r=0)= $E_0\frac{w_0}{w}$ [77], plugging in our E_0 value of 93.1 kV/cm (determined later).

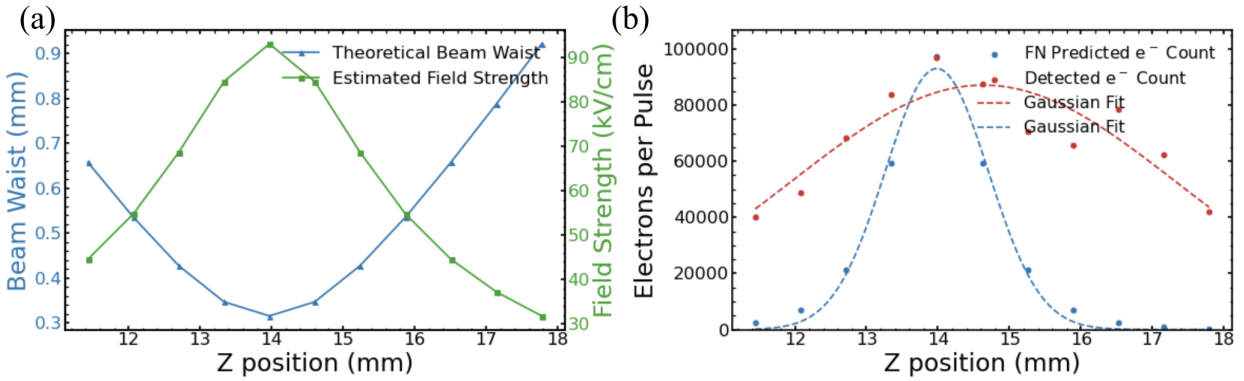

Figure 4.6: (a) THz Beam waist and estimated field strength as a function of Z position. (b) Detected electron counts as a function of Z vs. FN predicted electron count, with Gaussian fits superimposed.

Fig. 4.6(b) shows the comparison between the detected electron count and the predicted electron count, derived by plugging the theoretical field strengths into the FN equation. From this plot, it is clear that the real electron distribution is far too broad, indicating that

the THz beam does not conform to a Gaussian profile. This, along with other unexpected results that we discuss in the following chapter, raises further questions about air-plasma sources. To address these questions, a systematic study is needed, focusing on the effect of changing pulse compression and filament length on the shape of the focus.

4.2.1 Electron Energy Spectra

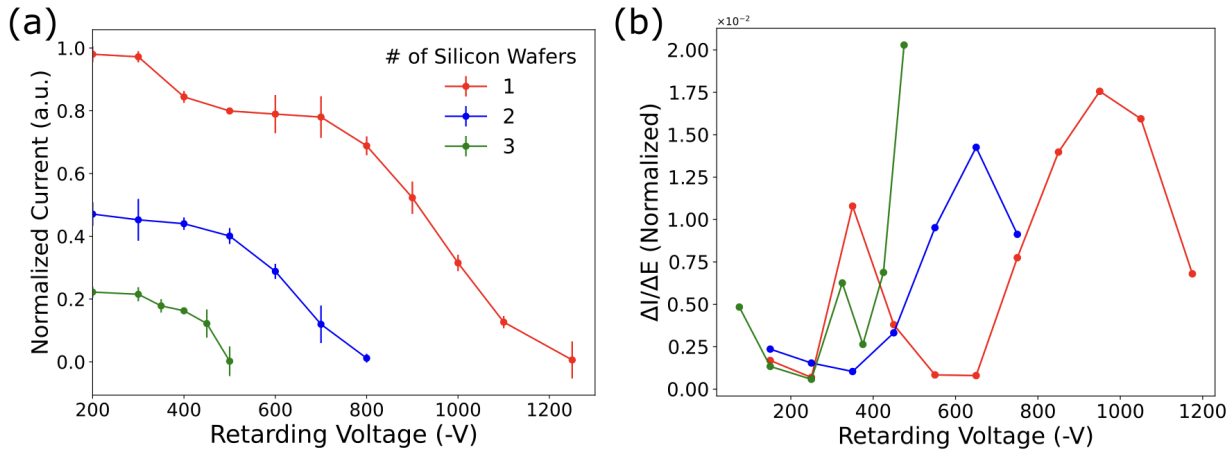

Figure 4.7: (a) Electron emission current measured at the Faraday cup detector as a function of the applied retarding potential for different incident fields, modulated by adding silicon wafers in the beam path. (b) Electron energy distributions derived from (a).

We now proceed to obtain an electron energy spectrum by applying a range of retarding voltages to the Faraday cup. These measurements, shown in Fig. 4.7 (a), were taken for a tip positioned at the center of the THz focus, located at : Z = 14 mm, Y = 10.7mm, X= 5.8mm. Here three sets of measurements were taken, with an extra silicon wafer introduced in the beam path to lower the incident field strength by 70% between sets of measurements.

These measurements were taken using a running loop to query the electrometer. For each iteration the electrometer returns a set of current values and their associated start times, with each current value being an integrative measurement of charge over time. The code then records these current measurements and their standard deviations across 5 loops, giving the error bars associated with the data points given above.

As we can see from 4.7 (b), the maximum electron energies detected are 1200eV, 800eV and 500eV, while the most commonly occurring energies are 950eV, 650eV and 475eV for 1, 2 and 3 wafers respectively. From these electron energies we can now determine the incident field strength using Eq. 2.4, which demonstrates analytically: $\Delta E \sim \frac{1}{4} e F_0 \lambda$. As this is a proportionality relationship, we can compare it with existing electron energy vs field strength data to obtain a empirical version. As part of their work, Matte *et al.* performed a similar energy scan using the same apparatus, however instead of using silicon wafers to modulate the field they used two wire-grid polarizers rotated relative to one another. Doing so they obtained the energy spectrum shown in Fig. 2.4 (c). Their field strengths were determined using EO sampling and were verified with several new crystals and displayed over-rotation and other behaviours associated with such high field strengths. While we also obtained field strength estimates from EO sampling, crystal aging and degradation from years of use have raised doubts about the validity of our EO sampling field strengths. Furthermore we did not experience over-rotation at the expected field strength and witnessed the crystal glowing red under illumination, which is known to result from defects in the ZnTe crystal [78]. For

this reason we prefer to point to these earlier field strength measurements and compare our known energies with theirs.

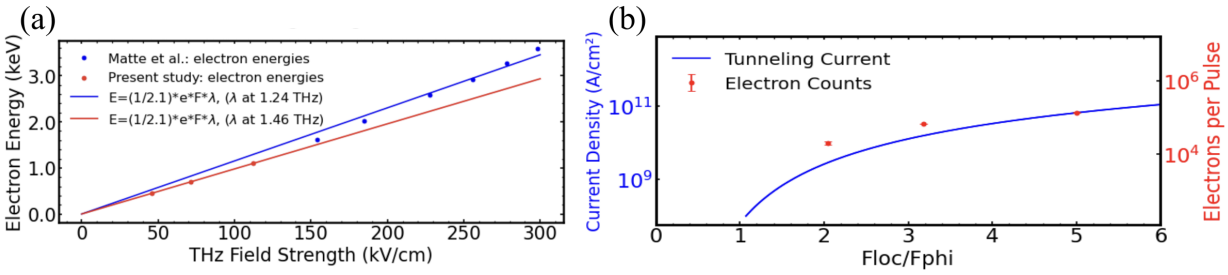

Figure 4.8: (a) Electron peak energy vs incident field strength, with data from present work in red and data taken from Matte in blue, with corresponding field strengths for peak energies. (b) THz local field vs emitted electrons per pulse and tunneling current given by FN tunneling theory. Observed data shown in red.

Recalling the relationship between electron energy and applied field given by $\Delta E \sim \frac{1}{4} e F_0 \lambda$, given in Eq. 2.4, if we look at Fig. 4.8 (a), we see that for the data of Matte *et al.*, equation 2.4, is better approximated by a replacing the factor of $\frac{1}{4}$ with a factor of $\frac{1}{2.1}$.

We then use this relationship to obtain our field strength estimates for our peak electron energies: 110, 70, 45 kV/cm for 1, 2 and 3 wafers respectively. If we account for the 70% transmission coefficient of silicon this gives our maximum THz field produced via air-plasma at $\approx$ 160 kV/cm, more than a factor of 4 less than our previous estimate derived from THz power. This further suggests that several pulses are arriving staggered in time rather than all at once.

We now compare our base electron currents and the above field strengths to FN emission theory. For the 3 field strengths given above we detect currents of 22.3, 11.1, 3.25 pA,

corresponding to 139x10^3, 69x10^3, 20x10^3 electrons per pulse respectively. Assuming an emission time of 0.4 ps, given by finite-difference time-domain simulation of our nanotip emission [8], and an emission area of 10 nm, also consistent with Matte et al, we obtain Fig. 4.8(b). From fitting our highest electron per pulse value onto the FN expected current line we obtain an estimate for the local field at the nanotip apex. As we can see this corresponds to a $\frac{F_{loc}}{F_\phi}$ coordinate of $\approx$ 4.4, as $F_\phi \approx 14GV/m$ for tungsten [79], this corresponds to a F_{loc} of 4.4x14 GV/m $\approx$ 62 GV/m. This gives a field enhancement $\gamma = 6000$. This value is considerably higher than those found in similar experiments. For example, Matte *et al.* presented several values obtained through different means, ranging from 1400-3800.

Another way to obtain an estimate of γ is by simulating ballistic acceleration of the electrons in the enhanced illuminating field. Doing so, and assuming the near field fall-off given by $\gamma(x) = \gamma/(1+2x/R)$ [5], we can model the dynamics of our highest energy electrons, emitted at the peak electric field, thus undergoing the maximum possible acceleration.

Using the 1-dimension finite-difference time-domain (FDTD) method, the simulation is broken into time steps where, at each step, the current position and velocity of the electron is updated. The code calculates the electric field at the current position, given by the spatial decay and the time slice within the passing pulse train shown in Fig. 4.9 (a), to determine the force acting on the electron. Using the calculated force, the electron's velocity and position are iteratively updated for each time step. The results, plotted as energy versus time for different tip radii are shown in Fig. 4.9 (b). The γ values were calculated using

the relationship $\gamma \sim 1/R$, with an initial gamma value of 1800 chosen for R = 30nm. As our tip radius is not precisely known, a range of tip radii and enhancement factors could have produced our detected electron energies of $\approx$ 1200 eV. As we can see, for our range of possible radii, our field enhancement estimate ranges from $\approx$ 1500 to 3500. Even this γ estimate of 3500 is significantly less than the estimate obtained from FN tunneling theory of 6000, and may be due to the presence of multiple pulses arriving staggered within our beam.

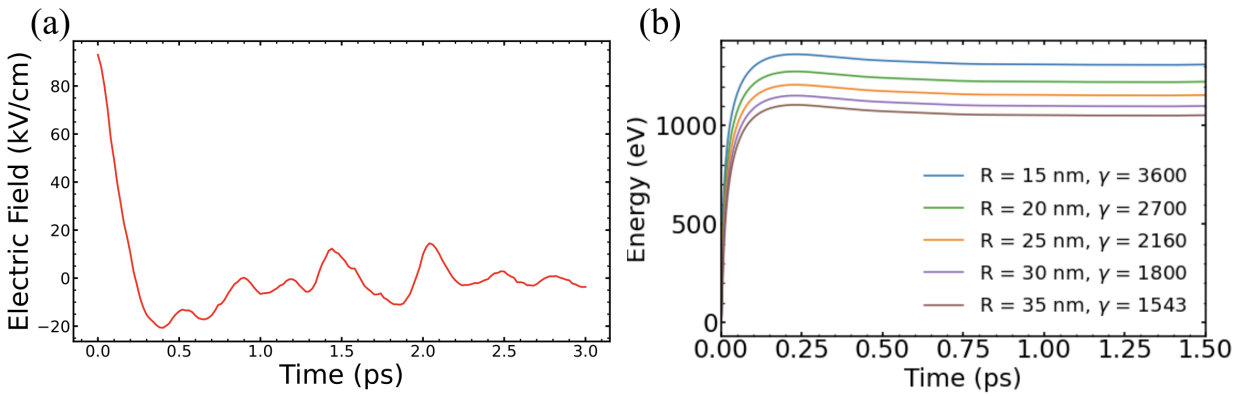

Figure 4.9: Results of classical 1D FDTD simulation. (a) driving THz field adapted from the waveform shown in Fig. 4.2, obtained using EO sampling. (b) Simulated electron energy as a function of time for varius radii, with scaled field-enhancement (γ) values.

While the γ estimate based on electron energy is directly linked to the highest incident field on the tip, and so would not be affected by this phenomenon, the same can not be said of our electron counts. In the FN estimation of γ above, we importantly assume the local field is present for a given period of 0.4 ps (a fraction of the positive cycle of our THz pulse). However, if this were no longer true, for example if several pulses were arriving with weaker fields rather than a single pulse, this would change our calculated γ. If we assume several

incident pulses, say 10 THz pulses with similar amplitudes per repetition rate of the laser, we would then obtain a γ of 3500, bringing it in line with the simulated values.

4.2.2 Comparison with EO data

Finally, we compare our electron emission Z-distribution to our EO sampling results. If we take the relative amplitudes of the pulses for each Z position of the EO crystal, taking the maximum peak to be 93.1kV/cm as found above, $\gamma = 6000$ and take the expected electron count per shot given by FN tunneling theory, we obtain Fig. 4.10 (a). If we then plot our maximum detected electron counts as a function of Z and compare with expected electron count we see a very different result, shown in Fig. 4.10 (b). As we can see from the measured THz fields we would expect a much narrower electron emission than was actually observed. This could be for a number of reasons which we will address one by one.

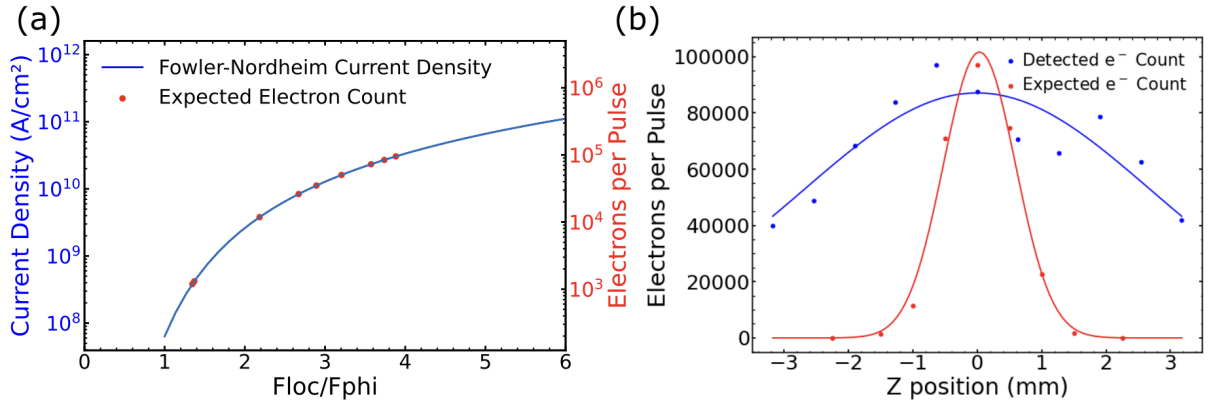

Figure 4.10: (a)Expected electron count given from known fields measured via EO sampling as a function of crystal position in Z and FN theory (b) Maximum detected electron counts as a function of Z vs expected electron count, with Gaussian fits superimposed.

First, the EO sampling signal and electron emission have very different frequency responses. As mentioned in Chapter 2.5, γ scales as $\frac{\lambda}{R}$, where R is the nanotip radius and λ is the wavelength of the incident light [5]. Meanwhile one of the reasons for which GaP is chosen for EO sampling is because of its relatively flat frequency response between 0 and 6 THz. This disparity in frequency responses likely played a role here, as we can see from figure 4.3 (b), the pulses measured across Z feature widely varying spectra, likely due to the λ-dependent focusing conditions and diffraction effects. We can account for this via post processing of our pulses, enhancing larger wavelengths in the spectrum and reconstructing the waveform. This post-processing involved transforming the original time-domain signals into the frequency domain using a Fast Fourier Transform (FFT). Each frequency component's amplitude was then adjusted by an enhancement factor that scales inversely with its frequency.

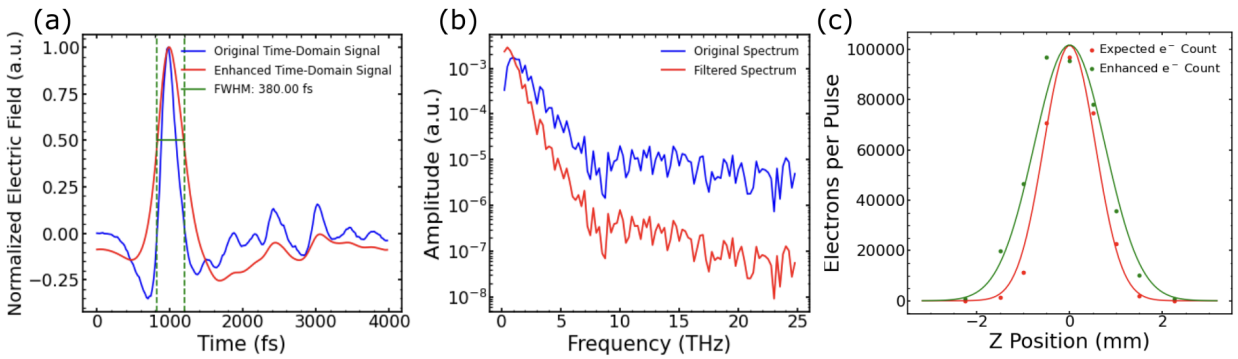

Figure 4.11: (a)Normalized time-domain traces of THz electric field at EO crystal position Z= -1.0mm, showing waveform before and after applying frequency filtering. (b) Normalized Fourier Transform of the time domain traces from (a) showing effect of frequency filtering. (c) Expected electron counts as a function of Z before and after enhancing lower frequencies with Gaussian fits superimposed.

The enhanced amplitude spectrum was then reconstructed back into the time-domain, ensuring that the resulting waveform was composed of real values. We also note the FWHM of the positive cycle of the pulse to account for longer or shorter electron emission times after filtering. Figure 4.11 illustrates an example waveform, from EO crystal position Z=-1.0mm, before and after low frequency enhancement. This effect was much more pronounced for large Z away from Z=0, as the differing focusing conditions become more visible further from the focal point of the mirror. Applying this enhancement of low frequencies and taking into account the different pulse FWHM and emission time we get Fig 4.11 (c). As we can see the expected electron emission distribution is less sharp in Z, however, this alone does not account for the disparity with observed data.

Another factor that we believe influenced our results is a systematic issue with the way

the EO sampling scan was taken. As the method requires co-focusing of both the THz and NIR beams, it is important that the two be perfectly overlapped, with the much smaller NIR beam interacting with the brightest part of the THz. This requires both optimization and refocusing of the NIR pulse for each Z position that was scanned. This was not done, however, as the 5mm hole in the OAPM through which the NIR passes precludes moving the lens forward as it would clip a larger percentage of the beam and influence our measurements that way. With this in mind we expect the size of the NIR focus on the crystal will change dramatically across Z simply because of the focusing conditions of a Gaussian beam.

In the same manner as earlier, we calculate the beam waist ($w(z)$) at various distances from the focus, and superimpose a ring of diameter equal to the calculated beam waist onto the electron emission Fig. 4.5 from before. This is shown in Fig. 4.12 (a).

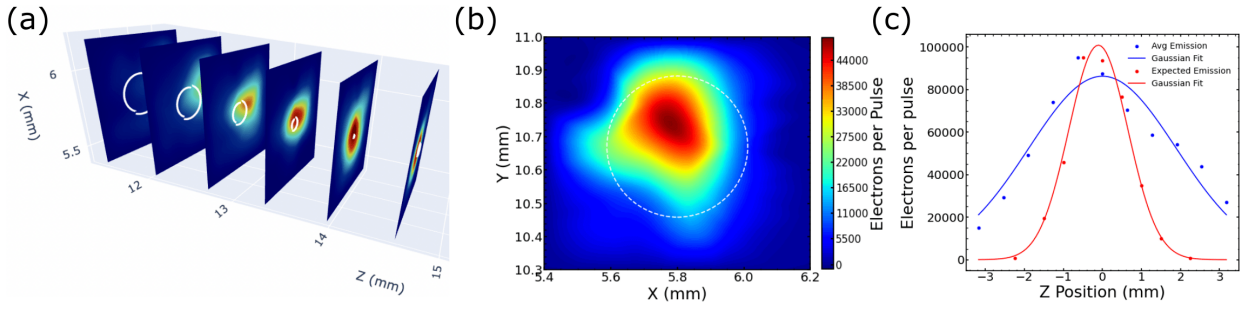

Figure 4.12: (a) Interpolated electron emission cross sections, with white circles showing calculated diameter of EO NIR probe pulse. (b) Single electron emission Z cut for Z = 17.8mm, with white circle showing region probed by EO NIR probe pulse. As we can see the highest electron emission recorded was 50x10^3 electrons per pulse, while the average emission for the circled region is 27x10^3. (c) Average detected electron counts in region of NIR probe as a function of Z vs expected electron count, with Gaussian fits superimposed.

As we can see the NIR beam waist expands to approximately the size of the THz beam for $Z >> z_R$, with $z_R = 80\mu m$. Thus the THz field being probed at these positions will be a mixture of field strengths that will contribute to produce a lower EO signal.

Once again we can take this effect into account by extracting the average electron emission in the region probed, as shown in Fig. 4.5 (b). For the example shown, at Z= 17.8mm doing so resulted in an electron emission of $27x10^3$ compared to the $50x10^3$ detected. Thus, for $Z >> z_R$ we can see this would result in a sharper electron emission as a function of Z, bringing it in line with our expectations. This is shown in Fig. 4.5 (c). While the two curves are still not matched, the difference in their FWHM's has gone from 4mm to 2mm. Other potential reasons for this disparity could be non co-linear NIR and THz beams during EO sampling. As is shown in Fig. 4.5 (a), we assume matching reference planes when comparing THz and NIR beam sizes as a function of Z, however if the beams were non-collinear, with the NIR beam moving further away from the central THz position while also expanding this would result in even lower detected fields than assumed.

Chapter 5

Modifications to Plasma Source

This chapter addresses modifications to the plasma source and outlines future work. We identified collimation issues in EO scans of the THz focus along the Z-axis. To resolve this, we propose using an axicon lens to replace the off-axis parabolic mirror (OAPM). Early experiments show improved beam focusing and reduced time delays. We detail the axicon lens design, its advantages over OAPM, and the positive impact on THz focus quality and electron emission characteristics, predicting enhanced electron energies and bunch charges from the modified plasma source.

5.1 Axicon Lens Collimation

As discussed in the previous chapter, while taking EO scans of the THz focus in Z, we noticed strange timing, in which several pulses were arriving staggered in time. This was

further validated by electron emission results, in which both the unexpectedly low electron energy and derived field strength, and high field enhancement pointed to this possibility.

We believe this issue stems from our use of an OAPM to collimate the beam, with only the THz emitted at the focal spot being perfectly imaged. Pulses that originate at the beginning or end of the plasma filament will not be perfectly collimated as shown in Fig. 5.1 (a). Consequently, they will feature different path lengths at the sample position. As this effect has not yet been reported in the literature, no solution has yet to be proposed. To this end, we have designed a collimating technique with an axicon lens to replace the collimating OAPM, as shown in Fig. 5.1(b).

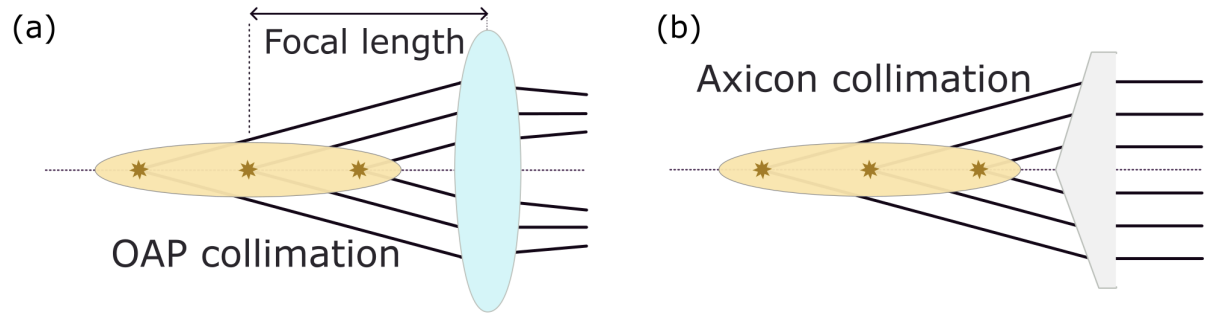

Figure 5.1: (a)Diagram of an OAPM, shown as a lens for simplicity, attempting to collimate a line source, effectively collimating only the beam emitted at the focal point. (b) Diagram depicting a line source collimated with an axicon lens. Figure adapted from[9].

The axicon lens, featuring a conical face and a flat exit surface, effectively collimates the THz beam produced by a long plasma filament. The angle of the conical face is calculated based on the material's index of refraction and the THz beam's emission angle. As detailed in Chapter 4.1.2, our found emission angle was not constant along the filament, with both

extremities having lower emission angles than the central region and an average emission angle of 6°. For a THz beam emitted at an angle φ, the angle θ of the conical surface is given by:

$$\theta = \arctan\left(\frac{n - \cos(\varphi)}{\sin(\varphi)}\right), \tag{5.1}$$

where n represents the refractive index of the axicon material at THz frequencies, generally ranging from 1.4 to 1.5 for the polymers utilized in this context [80].

The axicon lenses were crafted from commercially available high-density polyethylene (HDPE) or polytetrafluoroethylene (PTFE) rods using a lathe. These materials exhibit absorption at THz frequencies, so the lenses were constructed to be as thin as possible, about 1.5 mm, to preserve mechanical stability while minimizing absorption. These axicon lenses are mounted in a standard Thorlabs 2-inch holder. Some notable advantage of using axicon lenses over an OAPM is that the polymers scatter visible light, eliminating the need for a central hole in the mirror or additional filtering. This not only simplifies the initial setup but also reduces the overall material costs.

Early experiments have demonstrated notable improvement in the focusing of the beam and decreases in the observed time delay.

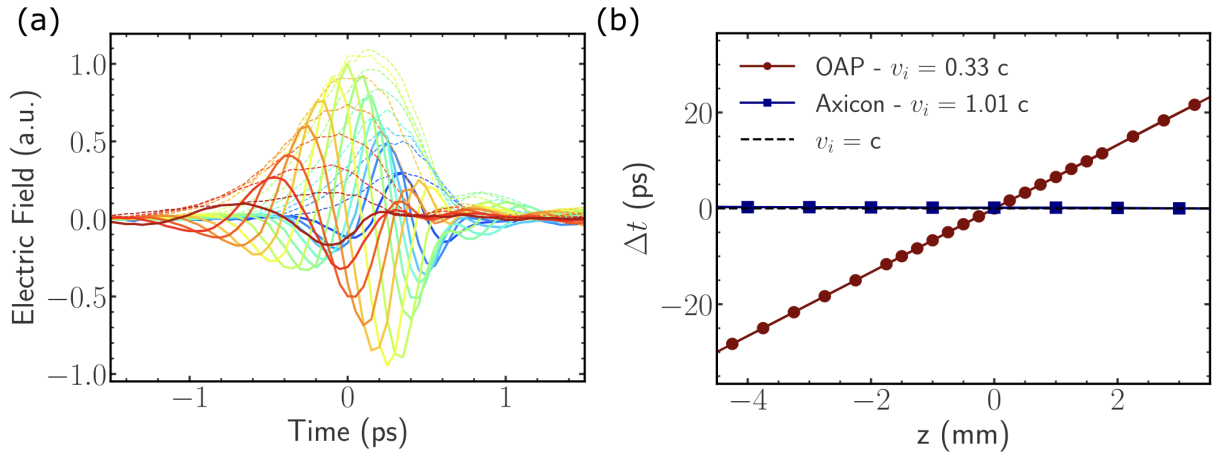

Figure 5.2: (a)Normalized time domain traces of the electric field as measured by a EO crystal positioned at different positions along the propagation axis using axicon lens. Dotted lines depict the electric field envelope. (b) Relative time-delay of the electric field peak vs EO crystal's position along the z-axis. Measurements using standard OAPM collimation are shown as blue circles, while those with the axicon are indicated with red squares. Solid lines represent the intensity front velocity.

The time-domain traces of the THz electric field using an axicon lens for collimation, rather than an OAPM, are shown in Figure 5.2 (a). Here, we see the time-delay observed in Fig. 4.3 from the OAPM collimation is almost completely absent. If we then examine the time delay as a function of the crystal position, we can calculate the velocity of the intensity front v_i using the eq:

$$\Delta t = \left(\frac{1}{v_i} - \frac{1}{c}\right) z \tag{5.2}$$

This result is shown in Fig. 5.2(b) for both the axicon and OAPM configurations. Here, a clear linear relationship appears, with $v_i = 0.33\,c$ for standard OAPM collimation, while the

axicon collimation provides an intensity front velocity of $v_i = 1.01\,c$, where the ideal case is $(v_i = c)$.

Currently, it's uncertain if this dephasing is inherent to all long-filament plasma THz sources. We believe it may be a result of optimizing THz power over the peak electric field, with imperfect or chirped pulses outputting higher average THz power [81, 82, 83]. Nonlinear optical properties and chirped laser pulses could also lead to the observed effect.

Another significant difference between axicon and OAPM lies in the quality of the observed THz focus. This effect is shown in Fig. 5.3. The FWHM shrinks from roughly 345 μm in the OAPM setup to under 200 μm with the axicon, reducing the transverse area to less than a quarter of its original size.

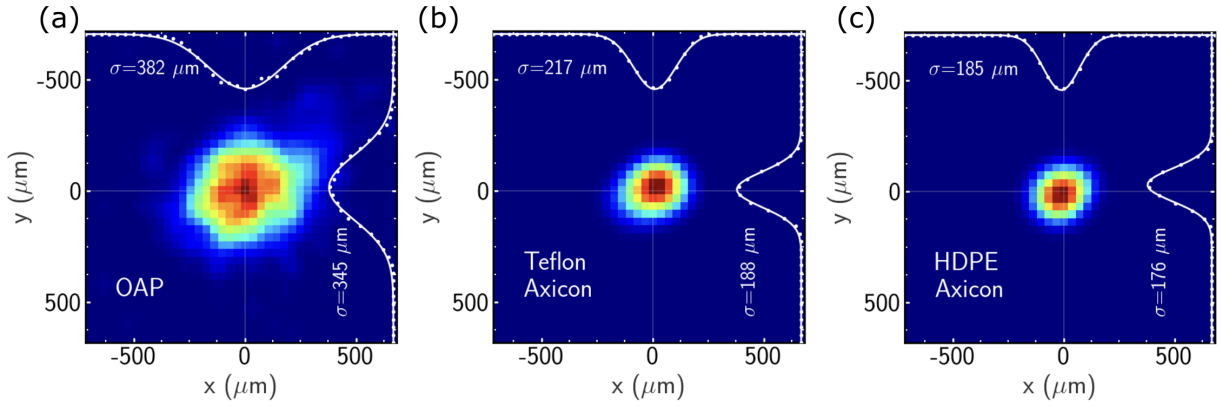

Figure 5.3: Images of the THz focus observed when using (a) a standard off-axis parabolic mirror (OAPM), (b) a Teflon axicon lens, and (c) a HDPE axicon lens. Each image presents horizontal and vertical cross-sections with their corresponding full-width at half-maximum values (σ). A Gaussian blur was of one pixel was applied for all images.

While it had been previously proposed that an axicon lens could theoretically refine

focusing [69], this is the first experimental confirmation. Furthermore, when comparing the focii produced when using HDPE and Teflon axicons we see a marked difference. This is due to HDPE's superior transmission of high frequencies [80] and the known scattering behavior of Teflon filters when transmitting THz radiation [84].

Finally, perhaps the most important improvement of the axicon collimation scheme was observed in the amplitude of the peak signal measured via EO sampling. When comparing to the OAPM configuration, the signal was also approximately 4 times larger, and given the signal modulation is directly proportional to the incident field strength, this suggests the field strength to be around 600 kV/cm. This would imply a field of 420 kV/cm incident at the tip when accounting for reflection occurring at the silicon window of our vacuum chamber. Using this estimate we can predict the electron count and energy we expect to see from our improved plasma source. The results of this are shown in Fig. 5.4. As we can see, for a field of 420 kV/cm, we expect electron energies of ≈ 5 keV, and bunch sizes of $3.8\text{x}10^6$ electrons. While the predicted electron energy is equal to the highest recorded CFE electron energy of 5 keV [5], the bunch charge exceeds the current CFE emission record of 10^6 [6] by a factor of 4.

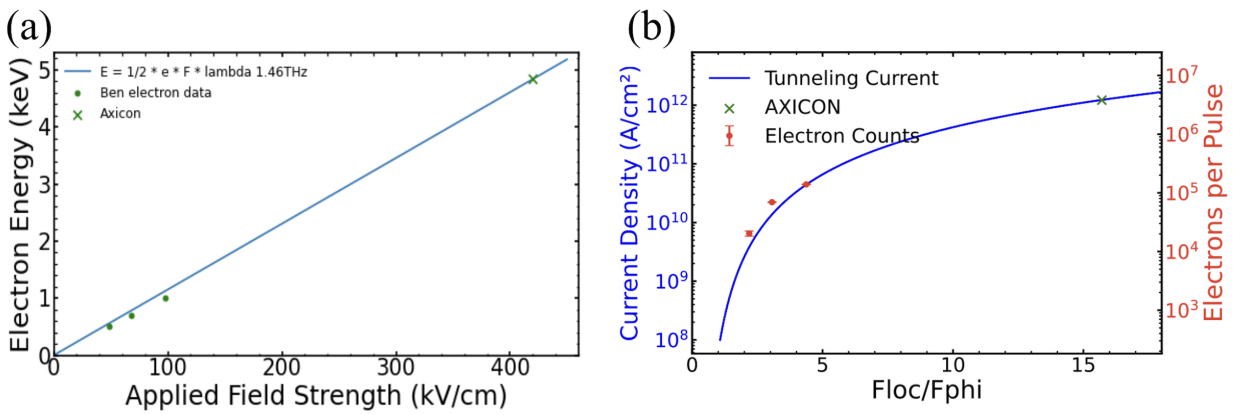

Figure 5.4: (a) Electron energy vs incident field strength of illuminating THz pulse. Data from OAPM collimation shown in red and expected data when using an axicon lens shown in green. (b) FN tunneling theory, with electrons per pulse vs local field, with observed data from OAPM in red and expected data when using an axicon lens shown in green.

While this experiment remains to be done, we expect to see a significant improvement over the existing source, demonstrating bunch charges well over 10^6. This advancement brings our electron source closer to our desired emission regime.

Chapter 6

A Novel Point-Projection Microscope

In this chapter we will briefly go over some important considerations and design aspects of a novel microscope to be constructed in the basement of Otto Mass Chemistry by Dec 2024. The first consideration is to isolate the system from molecular contamination as well as vibrational noise and stray fields. Each of these are separate problems that require individual solutions. The next consideration is usability and practical access of the microscope, where such things as sample manipulation, sample storage and turnaround time are considered.

6.1 Ultra-high Vacuum Chamber

We begin with a description of the vacuum system itself. While for the purposes of the experiment described in earlier sections of this text, a vacuum pressure of 10^{-6} Torr was acceptable, it was by no means ideal. At pressures of 10^{-6} Torr, considered 'high

vacuum' (HV), we experienced severe emission instability, likely due to the presence of nitrogen inside the chamber which coats the nanotip between emission cycles, forming a layer of tungsten nitrate. In the presence of high fields, field-assisted etching, in which tungsten nitrate molecules at the tip apex are ejected from the vicinity of the tip, leads to tip reshaping in irregular ways and unstable emission which varies over time [85]. This reshaping, as well as dentritic tungsten nitrate growth was observed by Matte *et al.* under similar conditions [6]. Sample contamination is also a crucial issue. In HV ($p \approx 10^{-6}$ Torr or approximately 1.3×10^{-6} mbar) and ultra high vacuum (UHV) ($p < 10^{-9}$ Torr or approximately 1.3×10^{-9} mbar), the monolayer formation time, τ, can be calculated using the equation [86]:

$$\tau = \frac{3.2 \times 10^{-6}}{p}\,\mathrm{s}$$

At high vacuum, the monolayer formation time is approximately 2.46 seconds. At 10^{-9} Torr, the monolayer formation time becomes significantly longer, approximately 2461.5 seconds (or about 41 minutes). For this reason it is necessary that we reach pressures in the UHV regime, as well as incorporating sample cleaning methods so as to maintain a clean surface during imaging.

Reaching 10^{-9} Torr requires several stages of pumping and careful consideration when designing the vacuum system. Below we describe our system as well as vacuum simulations done to ensure our system will reach UHV.

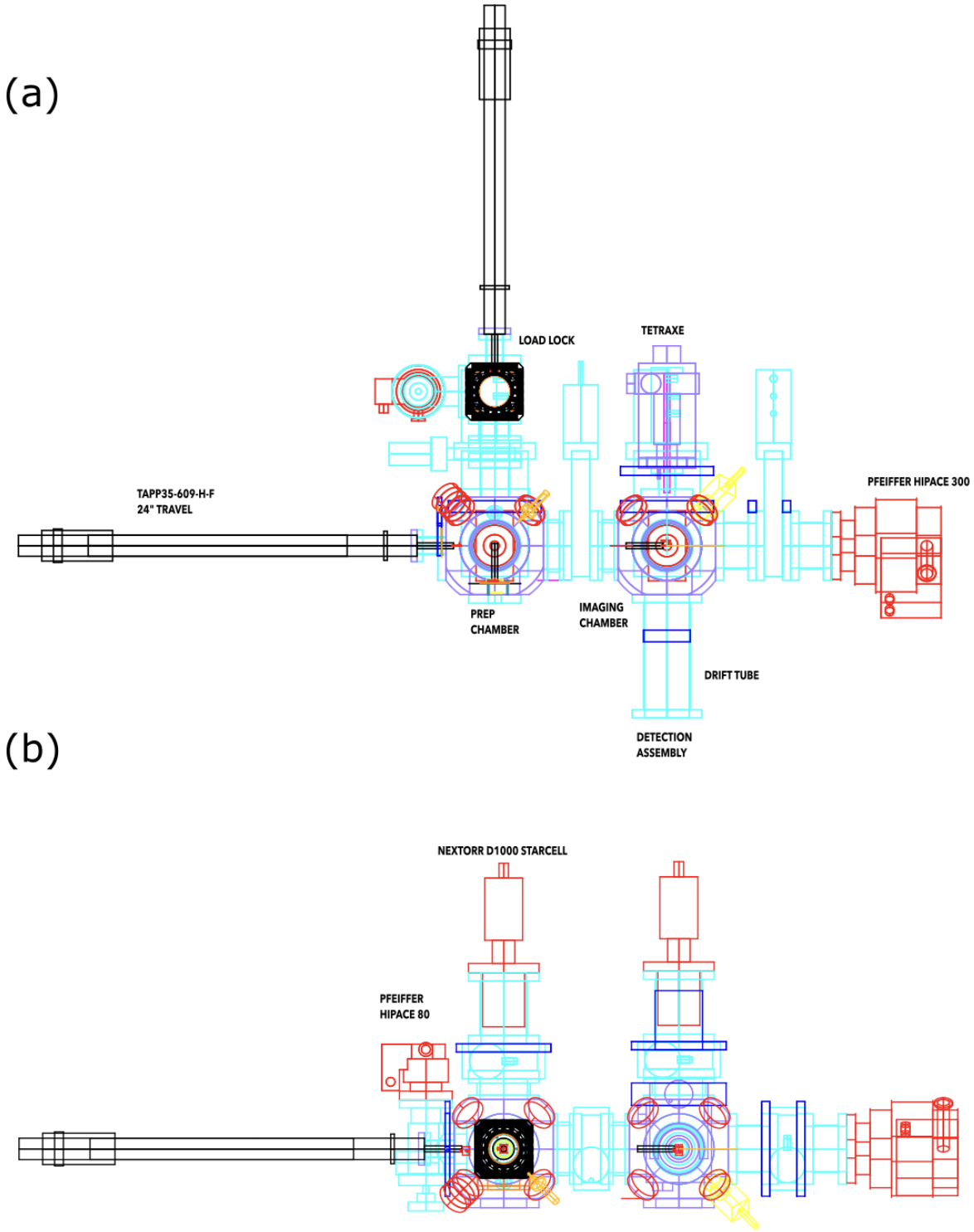

Figure 6.1: Diagram of our proposed UHV system with (a) side view and (b) top view.

In Fig 6.1 we show the latest design of the microscope and its vacuum system. The design was heavily influenced by a similar PPM built in 2012 at the University of Alberta in the group of Bob Wolkow [10]. Their system operated with a biased nanotip source emitting a constant current of 1.6 nA, with electron energies of 100–205 eV. While we make use of THz-driven bunched emission of keV electrons, the system remains largely the same. If anything, our higher electron energy will mean faster transit times and less sensitivity to Coulomb repulsion. The higher bunch charges also enable the possibility of single-shot imaging, which reduces sensitivity to mechanical vibrations. Otherwise, this microscope resembles theirs in nearly all aspects, with slightly different components due to budgeting reasons as well as technological improvements since 2012.

The core of the system is made up of 3 spherical cube chambers. The load-lock chamber, a MCF7450 4.50"CF chamber from Kimball Physics, is served by its own turbo pump, a Pfiffer HiPace 80, and will allow this section to be regularly brought to atmosphere and back to high vacuum. This section of the vacuum system is connected to the prep chamber, via a 2.37" coupling tube, through which a 28" TAPP35-609-H-F magnetically actuated triple-axis transfer arm will transfer the sample from the load-lock chamber to the sample prep. This whole section can be isolated by closing the neighbouring valves. All valves are manually actuated, unless otherwise stated, to prevent a surprise closure in the case of a power outage which could damage an extended transfer arm.

The sample prep chamber, MCF800 6.00"CF chamber from Kimball, features eight 1"

ports on its diagonals and six 6" ports on its sides. These many port options will be used to add functionalities in the future such as gas inlets, cryo fingers, residual pressure analyzers etc. For now, this chamber will be used for sample and tip preparation and cleaning as well as sample storage. It is independently pumped by a NEXTORR D1000 Starcell NEG-ION combination pump and will be held at UHV, except when introducing new samples or nanotips. The prep chamber may also be equipped with a field ion microscope (FIM) setup, which will be used to prepare our nanotips before use. The prep chamber is equipped with a 24" five-axis transfer arm, TAPP35-457-H-F, which can take the sample from the load-lock transfer arm or from a sample storage carousel and transfer it into the imaging chamber.

The imaging chamber, another MCF800, holds the microscope itself and will be pumped by both a Hipace 300M Turbo as well as a NEXTORR D1000. This larger turbo will pump both the imaging and prep chambers. In the event that the prep chamber alone must be brought to atmosphere, we may use the smaller turbo through the load lock arm to pump down the prep chamber before activating its ion pump. The imaging chamber will feature two unobstructed horizontal ports, with one used for light coupling to the tip and sample and the other for visual or manual access. A Tetraxe XYZ stage manipulator sits atop the imaging chamber and serves to control the position of the scanning head. Below the imaging chamber is the drift tube, a section lined with μ-metal to shield the electrons from magnetic fields as they propagate towards the detector assembly. The detector assembly is made up of a microchannel plate (MCP), phosphor screen and camera.

6.2 Simulating Vacuum Conditions

The most important consideration when calculating pumping speeds and final pressure are the volume of the region to be evacuated and the conductance of the system. Conductance is the measure of the capability of a vacuum system to transport gas from one area to another, and it is influenced by the geometry and dimensions of the vacuum components, such as pipes, valves, and fittings. Higher conductance implies less resistance to gas flow, thereby enabling faster evacuation. The effective pumping speed S_{eff} is related to the pumping speed S and the conductance C by [87]:

$$\frac{1}{S_{\text{eff}}} = \frac{1}{S} + \frac{1}{C} \tag{6.1}$$

Thus a low conductance will reduce the effective pumping rate significantly, rendering the speed of the pumps almost irrelevant if conductance is low. For this reason, when designing vacuum systems, a fundamental rule of thumb is to use wide tubing with no sudden changes in diameter to maximize the conductance. Bends should be minimized as they introduce resistance and reduce conductance, and any necessary transitions in diameter should be made as gradual as possible to avoid creating turbulence, which also reduces conductance [87].

The conductance of a straight tube in liters per second, at pressures below $\approx 10^{-3}$ Torr, can be calculated as follows [87]:

$$C = 12.1\frac{d^3}{l} \tag{6.2}$$

Where d is pipe inside diameter, l is the pipe length. For angle tubing elements, deviations can be taken into account by assuming a greater effective length l_{eff} and using the previous equation. This effective length is given by:

$$l_{eff} = l_{axial} + 1.33\frac{\Theta}{180^\circ}d \tag{6.3}$$

Where l_{axial} is the axial length of the line and Θ is the angle of the elbow (degrees of angle). Importantly, the conductances of each vacuum element add inversely as follows:

$$\frac{1}{C_{\text{total}}} = \sum_{i=1}^{n}\frac{1}{C_i} \tag{6.4}$$

The next consideration is the outgassing rate of the materials employed. All chambers are made of 316L stainless steel (SS), while the tubing is made of 304L SS. Both materials feature similar outgassing rates, after 14 hours of baking at 150°C, we estimate $\approx 5\times10^{-10}\frac{\text{Pa}\cdot\text{m}^3}{\text{s}\cdot\text{m}^2}$ [88]. Hydrogen permeation is another important consideration, with an estimated permeation rate of $10^{-16}\frac{\text{m}^2}{\text{s}}$ [89] for both steels. However, this estimate was found for steels produced via additive manufacturing, with other estimates between 10^{-13} and $10^{-15}\frac{\text{m}^2}{\text{s}}$ [90, 91].

To calculate outgassing and permeation rates we must also know the precise internal surface area of our system, as well as the volume. Below we will show a sample pump-down time calculation of a section of the system and leave the rest to appendix A.

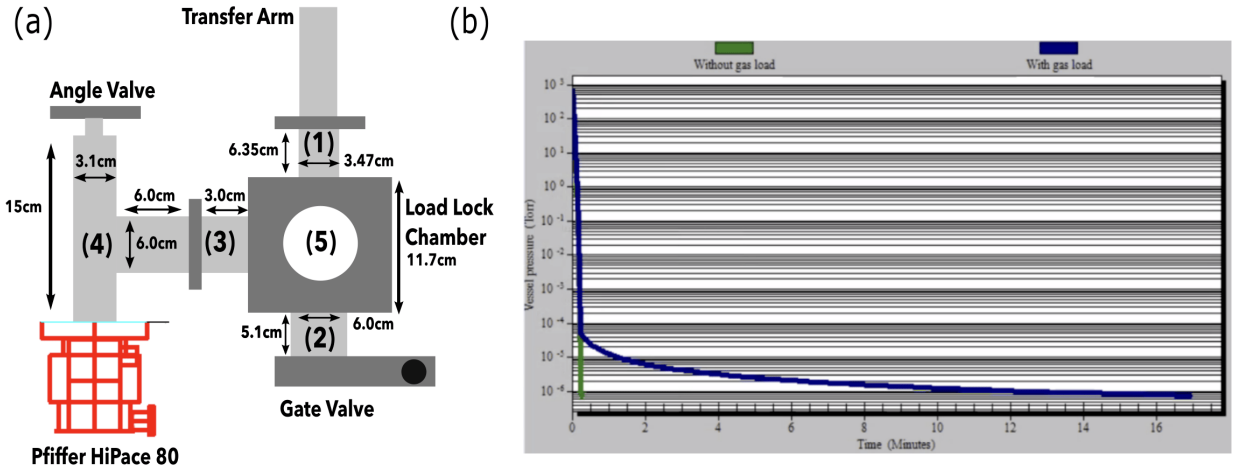

Figure 6.2: (a) Diagram of load-lock system, with relevant dimensions marked. (b) Vacuum pressure vs time in minutes for an ideal system and one with surface outgassing and hydrogen permeation. Plot produced using Vactran simulation software.

In Fig. 6.2 (a), we show the load-lock system with relevant sections numbered and dimensions marked. From here we extract the following values:

Table 6.1: System Volumes, Internal Surface Areas, and Conductance

Number	Volume (liters)	Surface Area (cm^2)	Conductance (liter/s)
1	0.0597	78.4	79.6
2	0.1442	124.4	512.5
3	0.179	119.7	435.6
4	0.643	439.2	136
5	0.4	450	1000[1]
System Total	1.416	1211	42.1

The conductance value of the chamber, given above as 1000[1], was estimated using its dimensions, but a precise value should be provided by the manufacturers. If we then calculate our S_{eff} given Eq. 6.4, using the HiPace base Nitrogen pumping speed of 67 l/s and the values

shown in Table 6.1, we end up with an effective pump speed S_{eff} of 25.9 l/s. Interestingly here doubling our pump's capacity to 130l/s would only bring this value to 31.8 l/s. Thus the system's entire pumping performance is determined by our choice of chambers, tubes, etc and not the pump itself. Here, the transfer arm was not included in the calculations as it is not clear how much interior surface area or volume is present and depends on the manufacturer to provide information. While this would present an added outgassing volume and a difficult region to pump it would likely not affect the pressures in the load-lock chamber significantly as it is so removed from the rest of the system. If it were at an extreme pressure differential, however, it could prove difficult to actuate the arm, though this remains to be seen.

If we then use the VacTran vacuum simulation software, inputting the values from Table 6.1 and the pumping information, we obtain the pump down plot shown in Fig. 6.2 (b), showing an expected pump down time of 16 minutes to reach 10^{-6} Torr. As we can see the effect of outgassing is significant at pressures around 10^{-4} Torr. As for other sections, including both imaging and prep chambers, we expect a pump-down time of 15 hours to reach a pressure of 10^{-10} Torr, for a permeation rate of $10^{-17}m^2/s$, while for the permeation rate of $10^{-16}m^2/s$ estimated above, the pressure is predicted to stabilize at 6x10^{-10} Torr after about 20 hours.

These estimates, while promising, are by no means final, with further adjustments to be made to the system's design and lingering questions about transfer arms as well as the true

permeation rate. These results can serve as a benchmark to compare the actual pump-down times of our system, once built, and if in disagreement, can point to unexpected issues such as micro-leaks or other. Overall this method of vacuum simulation offers results which are sensible and agree with the time scales seen in comparable vacuum systems. By careful design and consideration of vacuum fundamentals, as well as use of best practices when working with the instrument, we are confident the system will achieve the desired pressures for many years to come. For more information about these results and similar calculations see Appendix A.

6.3 Vibration Isolation and Scanning Head Design

The next important consideration when designing a microscope is vibration. While less of an issue if we achieve single-shot operation, any relative motion of the tip with the illuminating THz will cause emission instability. Furthermore relative motion between the tip and the sample, or the sample and the detector, between successive images will require complicated image alignment. We thus require several layers of vibration isolation, either passively or actively.

We begin by isolation of the vacuum system from the immediate environment, for which it is necessary to first ascertain the noise levels in the proposed area. For this, we had the company TMC Vibration Control perform a survey of the lab space, located in the basement of Otto Mass. They began by inspecting the site for stray AC magnetic fields, finding peaks

for all 3 axes: 44.5nT at 60.0Hz for Z, 4.45nT at 60Hz for Y, 18.9nT at 180Hz for X. These fields are orders of magnitude smaller than those produced by the Earth, usually between 20 and 65 μT at sea level [92] and thus should not pose an issue within the μ-metal drift tube.

TMC also manufacture the STACIS active isolation system, on which we considered placing the instrument. Vibration measurements were performed across the space at 5 points, with point 5 being the expected position of the microscope, with results shown in Fig. 6.3

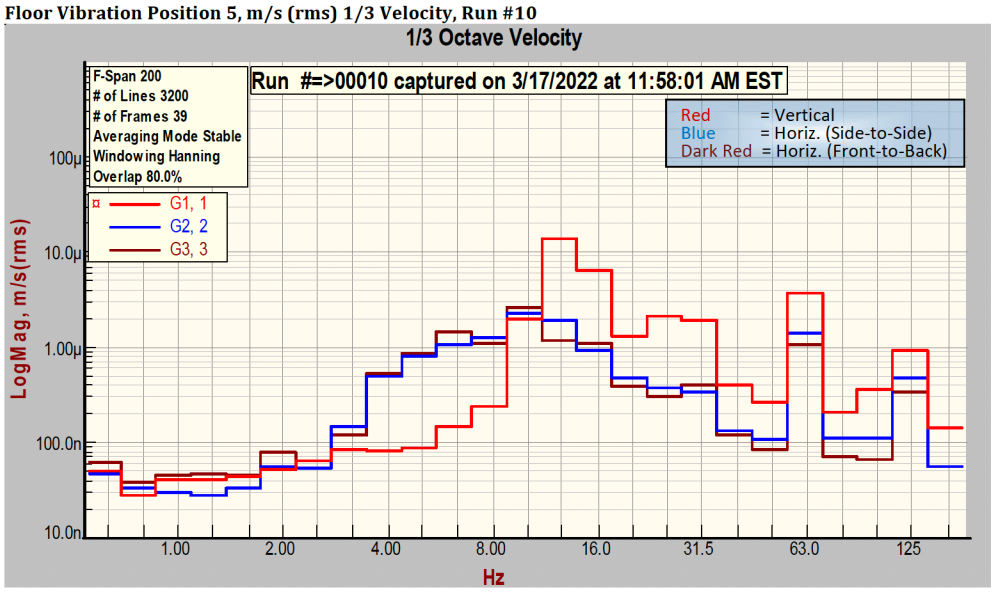

Figure 6.3: Results of vibration analysis in Otto Mass basement performed by TMC. Frequency is binned in bandwidth sections 1/3 octave wide.

We can then compare our vibration data to that published by Mutus *et al.* [10], with and without active STACIS isolation. In their case, the majority of the improvement from active isolation was in the low frequency range, below 5Hz, precisely where we report very little noise. In fact, our results show lower noise in this region than their instrument, even after

active isolation. In the region where we have the most vibration, from 8-25Hz, the STACIS system does very little. For this reason we have decided to forego active isolation, instead using pneumatic isolation, commonly found in optical tables for a fraction of the cost.

The next region in which vibration isolation is employed is in the scanning head design. The scanning head comprises the nanotip, the tip as well as the tip manipulation stages, held together inside the imaging chamber, in the configuration shown in Fig. 6.4 (a). The tip is hung upside down above the sample, and can be moved in X-Y-Z using 3 linear nano-positioners purchased from Attocube AG. Each of these linear stages have a coarse travel range of 5mm and a fine range of 3.5 µm, with step sizes of tens of nanometres. The position of the stages is read using a resistive sensor and is precise to 200nm. All stages are bakeable to 150°C and UHV compatible, with no magnetic materials used.

As tip-sample distances of 100's of nm are needed to achieve the desired magnifications, we need extreme precision in Z. Here, as both the sample and the stages on which the tip is mounted are affixed to the scanning head, relative motion of the two will be defined by the natural resonances of the stage stack.

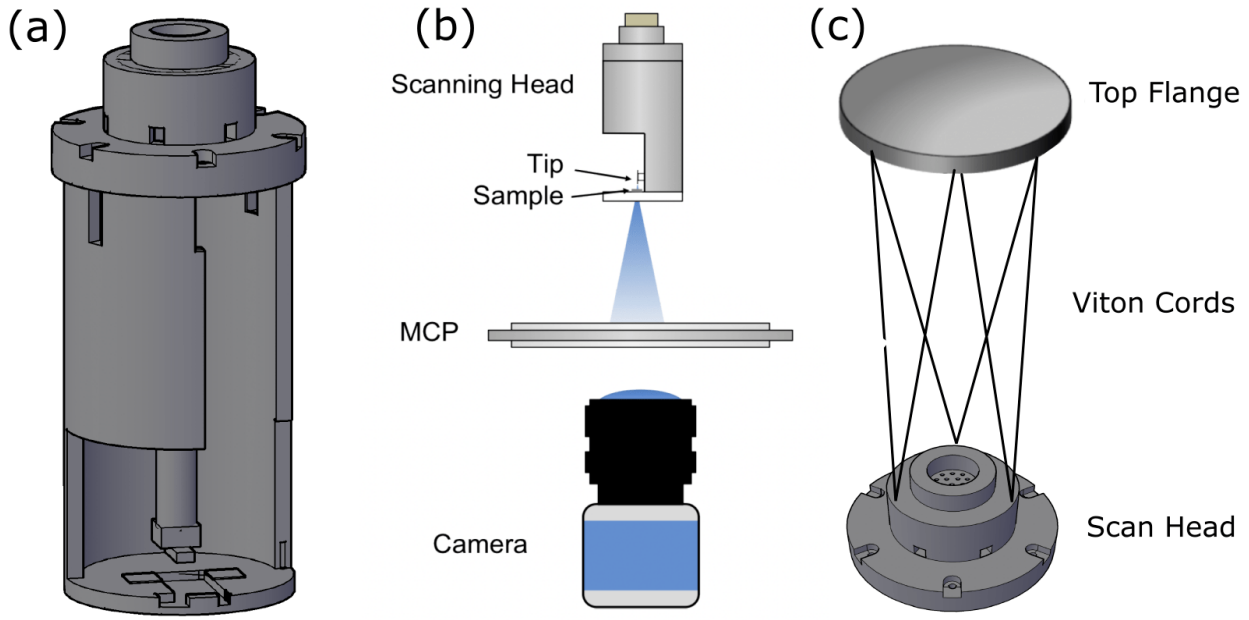

Figure 6.4: (a) Diagram of scanning head, inside of which XYZ sample manipulation stages control the tip position. (b) Diagram of imaging setup, in which the tip is held above the sample with electrons passing through the sample towards the detector assembly. Image adapted from [10] (c) Diagram of the scanning head suspension system, using Viton for vibration isolation and damping.

The scanning head is hung by 3 Viton chords to the ceiling flange for passive isolation, as shown in Fig. 6.4 (c). Viton, made of viscoelastic polymer, was chosen because it is UHV compatible and has excellent damping properties [93]. The Viton cord, threaded through the mounts on the scanner and the top flange, effectively dampens vibrations in the system, effectively isolating the scanning head. This setup was used by Mutus *et al.* and was shown to reduce noise levels to below 0.1 Å in relative motion between the tip and sample.

Chapter 7

Conclusion and Future Work

7.1 Summary

This thesis describes work done towards the advancement of a novel point-projection microscope, including experiments on air-plasma generated THz-driven electron emission sources, as well as novel findings about the plasma source itself. Before performing the experiments herein it was believed long filament two-colour plasma sources, with their high reported fields, would be an ideal source for CFE from tungsten nanotips. With field strength estimates based on Poynting flux in the MV/cm range, it was believed we could generate as many as 10^7 electrons per THz pulse.

We began by characterizing our THz source, finding an non-constant emission angle across the filament with an average of 6°. We also showed using EO sampling that our

pulse featured a unexpectedly low frequency distribution, with a central freq at 1.46 THz. We further showed using a microbolometer array camera the FWHM of the THz focus to be roughly 350 μm, with an average pulse energy of 186nJ. Using these estimates we calculated an estimated field strength of $\sim$ $700kV/cm$ using the Poynting flux method. We then employed our THz source for CFE and observed bunch sizes as high as 2x10^5 electrons per pulse, with energies reaching 1.3kV and a calculated field enhancement factor γ of 6000. Using the electron energy we have shown conclusively that the estimated fields obtained from power measurements were largely overestimated, with a more reasonable figure of $\sim$ 160 kV/cm being the true field strength. This discrepancy arises due to the initial use of an OAPM for collimation, which did not account for the varying path lengths and timing of pulses. Although the field strengths we measured are lower than anticipated, this constitutes a direct field measurement, representing a significant advancement over previous plasma-driven electron emission experiments. Those earlier studies used a bias voltage and reported THz fields of approximately 10 kV/cm [94, 4]. We also showed that the focus of our plasma source was inconsistent with that of a Gaussian beam, using the distribution of electron emission as a function of tip position in Z. This disagreed with previous suggestions [75] raising further questions about this source.

We have further shown that when working with long plasma filaments, approx 5 cm in length, poor collimation can lead to undesirable timing effects, in which multiple pulses arrive staggered in time. We believe this to be behind our lower than expected frequency

distribution, as well as our unexpectedly high field enhancement factor. We have proposed a method to resolve this issue using a collimating axicon lens to better manage the spatial and temporal focusing of the THz field. Early results have shown promise, with improvements in spatial distribution of the focus, with a focus FWHM of 200 μm, as well as a fourfold increase in electric field amplitude measured via EO sampling, suggesting fields of over 600 kV/cm.

With these improvements to our source, we propose that it may be possible to surpass the current emission record of 10^6 electrons, potentially generating up to 3.8x10^6 electrons per shot, with energies exceeding 5 keV.

In Chapter 6, we explored the design of a novel point-projection microscope set for construction by Dec 2024. We discussed steps taken to isolate the system from molecular contamination, vibrational noise, and stray fields while ensuring usability and practical access. Vacuum simulations were performed while designing the vacuum system, ensuring it will reach pressures below 10^{-9} Torr. Vibration isolation is achieved via a combination of passive pneumatic isolation and a Viton-based suspension system for the scanning head.

Overall, the instrument's thoughtful design and our promising electron emission results indicate it has the potential, with further advancements, to meet the desired specifications for single-shot operation. This development will pave the way for a point-projection microscope capable of pushing the boundaries of ultrafast imaging, offering groundbreaking discoveries in materials science and beyond.

7.2 Future Experiments

Our first proposed experiment involves using the new plasma source with the axicon lens to repeat the results of this thesis, measuring the new electron energies and bunch charge. This will validate the anticipated increase in field strength and further quantify the effectiveness of the axicon lens. Furthermore, with this experimental setup, we will strive to push beyond the existing electron emission records. These measurements will provide crucial insights into the future performance of our PPM and verify whether it can achieve single-shot operation. The successful execution of this experiment would establish the new standard for extremely bright ultrafast electron emission.

Our second proposed experiment aims to delve into the dynamics of electron emission using a novel autocorrelation setup to achieve sub-cycle temporal resolution. All our results thus far have been averaged over numerous emission cycles, leaving the finer dynamics unexplored. By using two THz pulses, each generated separately with one actively time-delayed relative to the other, we can observe the emission dynamics with unparalleled temporal precision. This THz streaking experiment will enable us to measure the replenishment rate of electron emission events and test for the presence of plasmonic responses of the material, shedding light on how these resonances influence electron emission and field enhancement. This method will provide insights into the transient electric field strength and its effects on electron dynamics, thereby allowing us to better understand the material's response to THz excitation and refine our models of CFE from

tungsten nanotips.

Another critical experiment involves employing a multi-channel plate (MCP) coupled with a phosphor screen to examine the spatial characteristics of the electron emission. By observing the distribution of emitted electrons on the phosphor screen while varying the incident field we can directly compare the emission patterns of different electron energies, verifying the effects of space charge and perhaps explore underlying physics of the source and its own electronic structure.

Furthermore, by inserting a sharp-edge object in the beam path and examining the interference pattern at the detector, we can characterize the spatial resolution of the source. This would allow us to fine-tune the emission source and optimize the imaging system before construction of the microscope. This groundwork will be pivotal in shaping the point-projection microscope's final design and ensuring its success.

Bibliography

[1] E. Quinonez, J. Handali, and B. Barwick, "Femtosecond photoelectron point projection microscope," *Review of Scientific Instruments*, vol. 84, p. 103710, 2013.

[2] M. Cheung, H. Adaniya, C. Cassidy, M. Yamashita, and T. Shintake, "Low-energy in-line electron holographic imaging of vitreous ice-embedded small biomolecules using a modified scanning electron microscope," *Ultramicroscopy*, vol. 209, p. 112883, Feb 2020. Epub 2019 Nov 4.

[3] S. Thomas, G. Wachter, C. Lemell, J. Burgdörfer, and P. Hommelhoff, "Large optical field enhancement for nanotips with large opening angles," *New Journal of Physics*, vol. 17, no. 6, p. 063010, 2015.

[4] G. Herink, L. Wimmer, and C. Ropers, "Field emission at terahertz frequencies: Actunneling and ultrafast carrier dynamics," *New Journal of Physics*, vol. 16, p. 123005, 2014.

[5] S. Li and R. R. Jones, "High-energy electron emission from metallic nano-tips driven by intense single-cycle terahertz pulses," *Journal Name*, vol. Volume Number, no. Issue Number, p. Page Numbers, 2016.

[6] D. Matte, N. Chamanara, L. Gingras, L. P. René de Cotret, T. L. Britt, B. J. Siwick, and D. G. Cooke, "Extreme lightwave electron field emission from a nanotip," *Physical Review Research*, vol. 3, p. 013137, Feb 2021. Published by the American Physical Society under the terms of the Creative Commons Attribution 4.0 International license. Further distribution of this work must maintain attribution to the author(s) and the published article's title, journal citation, and DOI.

[7] B. J. Dringoli, "Design and demonstration of an ultrafast terahertz spectrometer with femtosecond polarization-resolved detection capabilities," msc thesis, McGill University, Montréal, Québec, Canada, Aug. 2019.

[8] D. Matte, *Ultrafast Electron Cold Field Emission from a Tungsten Nanotip by Single Cycle THz Pulse*. Phd dissertation, McGill University, Montreal, Quebec, Canada, 4 2023. Supervised by David Cooke.

[9] R. T. Paulino, B. Colmey, and D. G. Cooke, "Spatiotemporal walk-off and improved focusing of plasma THz sources," *Opt. Express*, vol. 32, p. 26351–26358, Jul 2024.

[10] J. Mutus, *Low-Energy Electron Point Source Microscopy and Electron Holography*. 2012.

[11] E. Ruska, "Zur Fokussierbarkeit von Kathodenstrahlbündeln großer Ausgangsquerschnitte," *Zeitschrift für Physik*, vol. 83, no. 9, pp. 684–697, 1933.

[12] D. Gabor, "A new microscopic principle," *Nature*, vol. 161, no. 4098, pp. 777–78, 1948.

[13] R. E. Gordon, "Electron microscopy: a brief history and review of current clinical application," *PMID*, 2014.

[14] D. Strickland and G. Mourou, "Compression of Amplified Chirped Optical Pulses," *Optics Communications*, vol. 56, no. 3, pp. 219–221, 1985.

[15] J. C. Williamson, M. Dantus, S. B. Kim, and A. H. Zewail, "Ultrafast diffraction and molecular structure," *Chemical Physics Letters*, vol. 196, pp. 529–534, August 1992.

[16] B. J. Siwick, J. R. Dwyer, R. E. Jordan, and R. J. D. Miller, "An Atomic-Level View of Melting Using Femtosecond Electron Diffraction," *Science*, vol. 302, no. 5649, pp. 1382–1385, 2003.

[17] H. Ihee, J. Cao, and A. H. Zewail, "Ultrafast Electron Diffraction of Transient [Fe(CO)4]: Determination of Molecular Structure and Reaction Pathway," *Angewandte Chemie International Edition*, vol. 40, no. 8, pp. 1532–1536, 2001.

[18] I. Shafranovskii and N. Belov, *E. S. Fedorov*, p. 351. Springer, 1962.

[19] M. Pfeifer, G. Williams, I. Vartanyants, R. Harder, and I. Robinson, "Three-dimensional mapping of a deformation field inside a nanocrystal," *Nature*, vol. 442, pp. 63–66, 2006.

[20] R. E. Dunin-Borkowski *et al.*, "Electron holography," pp. 1141–95, 2019.

[21] G. Stevens, "Resolving power of lens-less low energy electron point source microscopy," *Journal of Microscopy*, vol. 235, no. 1, pp. 9–24, 2009.

[22] J. J. Thomson, "XL. Cathode Rays," *The London, Edinburgh, and Dublin Philosophical Magazine and Journal of Science*, vol. 44, no. 269, pp. 293–316, 1897.

[23] A. Einstein, "On a heuristic point of view toward the emission and transformation of light," *Ann. Phys*, vol. 17, p. 132, 1905.

[24] D. Filippetto, P. Musumeci, R. K. Li, B. J. Siwick, M. R. Otto, M. Centurion, and J. P. F. Nunes, "Ultrafast electron diffraction: Visualizing dynamic states of matter," *Rev. Mod. Phys.*, vol. 94, no. 4, p. 045004, 2022.

[25] J. D. Ewbank, J. Y. Luo, J. T. English, R. Liu, W. L. Faust, and L. Schäfer, "Time-resolved gas electron diffraction study of the 193-nm photolysis of 1,2-dichloroethenes," *The Journal of Physical Chemistry*, vol. 97, pp. 8795–8800, August 1993.

[26] A. H. Zewail, "Femtochemistry: Atomic-scale dynamics of the chemical bond," *The Journal of Physical Chemistry A*, vol. 104, no. 24, pp. 5660–5694, 2000. Available as PDF from tu-bs.de.

[27] C. M. Iaru, J. J. Geuchies, P. M. Koenraad, D. Vanmaekelbergh, and A. Y. Silov, "Strong carrier–phonon coupling in lead halide perovskite nanocrystals," *ACS Nano*, vol. 11, no. 11, pp. 11024–11030, 2017. https://doi.org/10.1021/acsnano.7b05033.

[28] P. Baum, "On the physics of ultrashort single-electron pulses for time-resolved microscopy and diffraction," *Chemical Physics*, vol. 423, pp. 55–61, 2013. `https://doi.org/10.1016/j.chemphys.2013.06.012`.

[29] B. W. Reed, "Femtosecond electron pulse propagation for ultrafast electron diffraction," *Journal of Applied Physics*, vol. 100, p. 034916, 2006. `https://doi.org/`.

[30] B. J. Siwick, J. R. Dwyer, R. E. Jordan, and R. J. D. Miller, "Ultrafast electron optics: Propagation dynamics of femtosecond electron packets," *Journal of Applied Physics*, vol. 92, pp. 1643–1648, 2002. `https://doi.org/10.1063/1.1487437`.

[31] S. B. van der Geer, M. J. de Loos, T. van Oudheusden, W. P. E. M. op 't Root, M. J. van der Wiel, and O. J. Luiten, "Longitudinal phase-space manipulation of ellipsoidal electron bunches in realistic fields," *Phys. Rev. ST Accel. Beams*, vol. 9, p. 044203, 2006. Published 26 April 2006.

[32] T. van Oudheusden, P. L. E. M. Pasmans, S. B. van der Geer, M. J. de Loos, M. J. van der Wiel, and O. J. Luiten, "Compression of subrelativistic space-charge-dominated electron bunches for single-shot femtosecond electron diffraction," *Phys. Rev. Lett.*, vol. 105, p. 264801, 2010. Published 22 December 2010.

[33] A. Rose, "The sensitivity performance of the human eye on an absolute scale," *Journal of the Optical Society of America*, vol. 38, no. 2, pp. 196–208, 1948.

[34] T. LaGrange, M. R. Armstrong, K. Boyden, C. G. Brown, G. H. Campbell, J. D. Colvin, W. J. DeHope, A. M. Frank, D. J. Gibson, F. V. Hartemann, J. S. Kim, W. E. King, B. J. Pyke, B. W. Reed, M. D. Shirk, R. M. Shuttlesworth, B. C. Stuart, B. R. Torralva, and N. D. Browning, "Single-shot dynamic transmission electron microscopy," *Appl. Phys. Lett.*, vol. 89, p. 044105, July 2006.

[35] R. K. Li and P. Musumeci, "Single-shot mev transmission electron microscopy with picosecond temporal resolution," *Phys. Rev. Applied*, vol. 2, p. 024003, August 2014.

[36] J. Vogelsang, G. Hergert, D. Wang, P. Groß, and C. Lienau, "Observing charge separation in nanoantennas via ultrafast point-projection electron microscopy," *Light: Science & Applications*, vol. 7, p. 55, 2018. Official journal of the CIOMP.

[37] G. A. Morton and E. G. Ramberg, "Point projector electron microscope," *Physical Review*, vol. 56, p. 705, 1939.

[38] J. Spence and J. Cowley, "Electron holography at low energy," in *Introduction to Electron Holography* (E. V"olkl, L. Allard, and D. Joy, eds.), Plenum Pub Corp, 1999.

[39] M. Born and E. Wolf, *Principles of Optics*, ch. 4.8.2. Stops and pupils, p. 852. United Kingdom: Pergamon Press, 60th anniversary edition ed., 2019.

[40] F. Ardana-Lamas, F. L. Pimpec, A. Anghel, and C. P. Hauri, "Towards high brightness electron beams from multifilamentary nb_3sn wire photocathode," *Phys. Rev. ST Accel. Beams*, vol. 16, p. 043401, April 2013.

[41] M. Reiser, *Theory and Design of Charged Particle Beams*. Weinheim: WILEY-VCH Verlag GmbH & Co. KGaA, 2008.

[42] A. Arbouet, G. M. Caruso, and F. Houdellier, "Ultrafast transmission electron microscopy: Historical development, instrumentation, and applications," *Advances in Imaging and Electron Physics*, 2018.

[43] N. Boroumand, A. Thorpe, A. M. Parks, and T. Brabec, "Keldysh ionization theory of atoms: mathematical details," *J. Phys. B: At. Mol. Opt. Phys.*, vol. 55, p. 213001, 2022. 10pp.

[44] S. S. Wellershoff, J. Hohlfeld, J. Güdde, and E. Matthias, "The role of electron-phonon coupling in femtosecond laser damage of metals," *Appl. Phys. A-Mater.*, vol. 69, p. S99, 1999.

[45] R. H. Fowler and L. Nordheim, "Electron emission in intense electric fields," *Proceedings of the Royal Society of London. Series A, Containing Papers of a Mathematical and Physical Character*, vol. 119, no. 781, pp. 173–181, 1928.

[46] S. L. Lange, N. K. Noori, T. M. B. Kristensen, K. Steenberg, and P. U. Jepsen, "Ultrafast thz-driven electron emission from metal metasurfaces," *Journal of Applied Physics*, vol. 128, no. 7, p. 070901, 2020.

[47] R. G. Forbes and J. H. B. Deane, "Comparison of approximations for the principal Schottky–Nordheim barrier function v(f), and comments on Fowler–Nordheim plots," *Journal of Vacuum Science & Technology B*, vol. 28, no. 2, pp. C2A33–C2A42, 2010.

[48] S. Kim, J. Jin, Y.-J. Kim, I.-Y. Park, Y. Kim, and S.-W. Kim, "High-harmonic generation by resonant plasmon field enhancement," *Nature*, vol. 453, no. 7196, pp. 757–760, 2008.

[49] M. K. Miller, A. Cerezo, M. G. Hetherington, and G. D. W. Smith, *Atom Probe Field Ion Microscopy*. Monographs on the Physics and Chemistry of Materials, Oxford: Oxford University Press, 1996.

[50] S. Podenok, M. Sveningsson, K. Hansen, and E. E. B. Campbell, "Electric field enhancement factors around a metallic, end-capped cylinder," *Nano*, vol. 1, pp. 87–93, 2006.

[51] J. H. Kang, D. S. Kim, and Q. H. Park, "Local capacitor model for plasmonic electric field enhancement," *Phys. Rev. Lett.*, vol. 102, p. 093906, 2009.

[52] C. Hernandez Garcia and C. A. Brau, "Pulsed photoelectric field emission from needle cathodes," *Nuclear Instruments and Methods in Physics Research Section A: Accelerators, Spectrometers, Detectors and Associated Equipment*, vol. 483, pp. 273–276, May 2002.

[53] P. Hommelhoff, C. Kealhofer, and M. A. Kasevich, "Ultrafast Electron Pulses from a Tungsten Tip Triggered by Low-Power Femtosecond Laser Pulses," *Physical Review Letters*, vol. 97, no. 24, p. 247402, 2006.

[54] C. Kealhofer, W. Schneider, D. Ehberger, A. Ryabov, F. Krausz, and P. Baum, "All-optical control and metrology of electron pulses," *Science*, vol. 352, no. 6284, pp. 429–433, 2016.

[55] D. G. Cooke, *Time-resolved terahertz spectroscopy of bulk and nanoscale semiconductors*. Ph.d. thesis, 2007.

[56] R. W. Boyd, *Nonlinear Optics*. Elsevier, 2003.

[57] S. Vidal, J. Degert, M. Tondusson, E. Freysz, and J. Oberlé, "Optimized terahertz generation via optical rectification in znte crystals," *Journal of the Optical Society of America B*, vol. 31, no. 1, pp. 149–153, 2014.

[58] M. Nakamura, S. Higuchi, S. Takekawa, K. Terabe, Y. Furukawa, and K. Kitamura, "Optical damage resistance and refractive indices in near-stoichiometric mgo-doped

linbo3," *Japanese Journal of Applied Physics*, vol. 41, no. Part 2, No. 1A/B, pp. L49–L51, 2002.

[59] J. Hebling, A. Stepanov, G. Almási, B. Bartal, and J. Kuhl, "Tunable thz pulse generation by optical rectification of ultrashort laser pulses with tilted pulse fronts," *Applied Physics B*, vol. 78, no. 5, pp. 593–599, 2004.

[60] J. A. Fülöp, L. Pálfalvi, G. Almási, and J. Hebling, "Design of high-energy terahertz sources based on optical rectification," *Optics Express*, vol. 18, no. 12, pp. 12311–12327, 2010.

[61] H. Hirori, A. Doi, F. Blanchard, and K. Tanaka, "Single-cycle terahertz pulses with amplitudes exceeding 1 mv/cm generated by optical rectification in linbo3," *Applied Physics Letters*, vol. 98, no. 9, p. 091106, 2011.

[62] M. Kress *et al.*, "Terahertz-pulse generation by photoionization of air with laser pulses composed of both fundamental and second-harmonic waves," *Optics Letters*, vol. 29, pp. 1120–1122, May 2004.

[63] D. J. Cook and R. M. Hochstrasser, "Intense terahertz pulses by four-wave rectification in air," *Optics Letters*, vol. 25, no. 16, pp. 1210–1212, 2000.

[64] K. Y. Kim *et al.*, "Terahertz emission from ultrafast ionizing air in symmetry-broken laser fields," *Optics Express*, vol. 15, pp. 4577–4584, Apr 2007.

[65] Z. Zhang *et al.*, "Controllable terahertz radiation from a linear-dipole array formed by a two-color laser filament in air," *Physical Review Letters*, vol. 117, p. 243901, Dec 2016.

[66] V. Y. Fedorov, A. D. Koulouklidis, and S. Tzortzakis, "Thz generation by two-color femtosecond filaments with complex polarization states: Four-wave mixing versus photocurrent contributions," *Plasma Physics and Controlled Fusion*, vol. 59, no. 1, p. 014025, 2016.

[67] J.-M. Manceau, M. Massaouti, and S. Tzortzakis, "Coherent control of thz pulses polarization from femtosecond laser filaments in gases," *Optics Express*, vol. 18, pp. 18894–18899, Aug. 2010.

[68] M. Clerici, M. Peccianti, B. E. Schmidt, L. Caspani, M. Shalaby, M. Giguère, A. Lotti, A. Couairon, F. Légareé, T. Ozaki, D. Faccio, and R. Morandotti, "Wavelength scaling of terahertz generation by gas ionization," *Physical Review Letters*, vol. 110, no. 25, p. 253901, 2013.

[69] T. I. Oh, Y. S. You, N. Jhajj, E. W. Rosenthal, H. M. Milchberg, and K. Y. Kim, "Intense terahertz generation in two-color laser filamentation: Energy scaling with terawatt laser systems," *New Journal of Physics*, vol. 15, p. 075002, jul 2013.

[70] A.-S. Lucier, "Preparation and characterization of tungsten tips suitable for molecular electronics studies," msc thesis, McGill University, Montréal, Québec, Canada, Feb. 2004.

[71] P. C. M. Planken, H.-K. Nienhuys, H. J. Bakker, and T. Wenckebach, "Measurement and calculation of the orientation dependence of terahertz pulse detection in ZnTe," *Journal of the Optical Society of America B*, vol. 18, no. 3, pp. 313–317, 2001.

[72] D. S. Sitnikov, S. A. Romashevskiy, A. V. Ovchinnikov, O. V. Chefonov, A. B. Savel'ev, and M. B. Agranat, "Estimation of THz field strength by an electro-optic sampling technique using arbitrary long gating pulses," *Laser Physics Letters*, vol. 16, no. 11, p. 115302, 2019.

[73] I.-C. Ho, X. Guo, and X.-C. Zhang, "Design and performance of reflective terahertz air-biased-coherent-detection for time-domain spectroscopy," *Opt. Express*, vol. 18, pp. 2872–2883, Feb 2010.

[74] D. S. Sitnikov, S. A. Romashevskiy, A. V. Ovchinnikov, O. V. Chefonov, A. B. Savel'ev, and M. B. Agranat, "Estimation of thz field strength by an electro-optic sampling technique using arbitrary long gating pulses," *Laser Physics Letters*, vol. 16, no. 11, p. 115302, 2019. Published 24 October 2019.

[75] C. B. Sørensen, L. Guiramand, J. Degert, M. Tondusson, E. Skovsen, E. Freysz, and E. Abraham, "Conical versus gaussian terahertz emission from two-color laser-induced air plasma filaments," *Optics Letters*, vol. 45, no. 7, pp. 2132–2135, 2020.

[76] R. Paschotta, "Gaussian beams." RP Photonics Encyclopedia, 2024. Retrieved April 26, 2024.

[77] O. Svelto, *Principles of Lasers*. New York: Springer/Sci-Tech/Trade, 5th ed., 2009. See page 153.

[78] M. A. Baghchesara, M. Cheraghizade, and R. Yousefi, "Growth and characterization of znte nanowires grown in a large scale by a cvd method," *Materials Letters*, vol. 162, pp. 195–198, January 2016.

[79] R. G. Forbes, "Description of field emission current/voltage characteristics in terms of scaled barrier field values (γ-values)," *J. Vac. Sci. Technol. B*, vol. 26, no. 1, pp. 209–213, 2008. Research Article.

[80] V. E. Rogalin, I. A. Kaplunov, and G. I. Kropotov, "Optical Materials for the THz Range," *Optics and Spectroscopy*, vol. 125, pp. 1053–1064, Dec. 2018.

[81] Z. Zhang, N. Panov, V. Andreeva, Z. Zhang, A. Slepkov, D. Shipilo, M. D. Thomson, T.-J. Wang, I. Babushkin, A. Demircan, U. Morgner, Y. Chen, O. Kosareva, and A. Savel'ev, "Optimum chirp for efficient terahertz generation from two-color femtosecond pulses in air," *Applied Physics Letters*, vol. 113, p. 241103, Dec. 2018.

[82] L. Zhang, L. Z. Ji, P. Y. Sun, Z. H. Jiao, S. F. Zhao, and G. L. Wang, "Enhanced terahertz generation by controlling electron trajectory with chirp laser field," *Indian Journal of Physics*, vol. 98, pp. 763–770, Feb. 2024.

[83] A. Martinez, J. Houard, A. Hideur, D. Paparo, and A. Vella, "Controlling the time shape of terahertz pulses from two-color plasma by combining wavelength dispersion and laser chirp," *Applied Physics Letters*, vol. 124, p. 021105, Jan. 2024.

[84] T. I. Oh, Y. J. Yoo, Y. S. You, and K. Y. Kim, "Generation of strong terahertz fields exceeding 8 MV/cm at 1 kHz and real-time beam profiling," *Applied Physics Letters*, vol. 105, p. 041103, July 2014.

[85] M. Rezeq, J. Pitters, and R. Wolkow, "Tungsten nanotip fabrication by spatially controlled field-assisted reaction with nitrogen," *Journal of Chemical Physics*, vol. 124, p. 204716, 2006.

[86] O. L. Vacuum, *Fundamentals of Vacuum Technology*. Cologne: Oerlikon Leybold Vacuum, 2007. Kat.-Nr. 199 90.

[87] D. Hoffman, B. Singh, and J. H. Thomas III, *Handbook of Vacuum Science and Technology*. Elsevier, 1997.

[88] Y. Ishikawa, Y. Koguchi, and K. Odaka, "Outgassing rate of some austenitic stainless steels," *Journal of Vacuum Science & Technology A*, vol. 9, pp. 250–253, 1991.

[89] J. Lin, F. Chen, F. Liu, D. Xu, J. Gao, and X. Tang, "Hydrogen permeation behavior and hydrogen-induced defects in 316l stainless steels manufactured by additive manufacturing," *Materials Chemistry and Physics*, 2020.

[90] P. Kumar and R. Balasubramaniam, "Determination of hydrogen diffusivity in austenitic stainless steels by subscale microhardness profiling," *Journal of Alloys and Compounds*, vol. 243, no. 1-2, pp. 249–258, 1996.

[91] M. Duportal, A. Oudriss, X. Feaugas, and C. Savall, "On the estimation of the diffusion coefficient and distribution of hydrogen in stainless steel," *Scripta Materialia*, vol. 186, pp. 352–355, 2020.

[92] C. C. Finlay, S. Maus, C. D. Beggan, T. N. Bondar, A. Chambodut, T. A. Chernova, A. Chulliat, V. P. Golovkov, B. Hamilton, M. Hamoudi, R. Holme, G. Hulot, W. Kuang, B. Langlais, V. Lesur, F. J. Lowes, H. Lühr, S. Macmillan, M. Mandea, S. McLean, C. Manoj, M. Menvielle, I. Michaelis, N. Olsen, J. Rauberg, M. Rother, T. J. Sabaka, A. Tangborn, L. Tøffner-Clausen, E. Thébault, A. W. P. Thomson, I. Wardinski, Z. Wei, and T. I. Zvereva, "International geomagnetic reference field: the eleventh generation," *Geophysical Journal International*, vol. 183, no. 3, pp. 1216–1230, 2010.

[93] J. A. Miwa, J. M. MacLeod, A. Moffat, and A. B. McLean, "Rattling modes and the intrinsic vibrational spectrum of beetle-type scanning tunneling microscopes," *Ultramicroscopy*, vol. 98, no. 1, pp. 43–49, 2003.

[94] M. Karam, J. Houard, G. Damarla, L. Rousseau, O. Bhorade, and A. Vella, "Thz driven field emission: energy and time-of-flight spectra of ions," *New Journal of Physics*,

vol. 25, p. 113017, 2023. Published on behalf of the Institute of Physics and Deutsche Physikalische Gesellschaft.

Appendix A

Additional Vacuum Simulations

Here we present further calculations and pumping simulations for our vacuum system, continuing from section 6.2. In Fig. A.1, we see a diagram with dimensions of the entire vacuum system except the load-lock. The system can be considered as one or two separate sections, (a) and (b), made up of the prep and imaging chamber respectively, isolated from one another by an in-line valve. It is necessary to consider them as one section when calculating time to reach high vacuum as they are serviced by a shared turbo pump. As for calculating time to reach UHV it is possible to calculate each separately as they are independently serviced by two ion pumps.

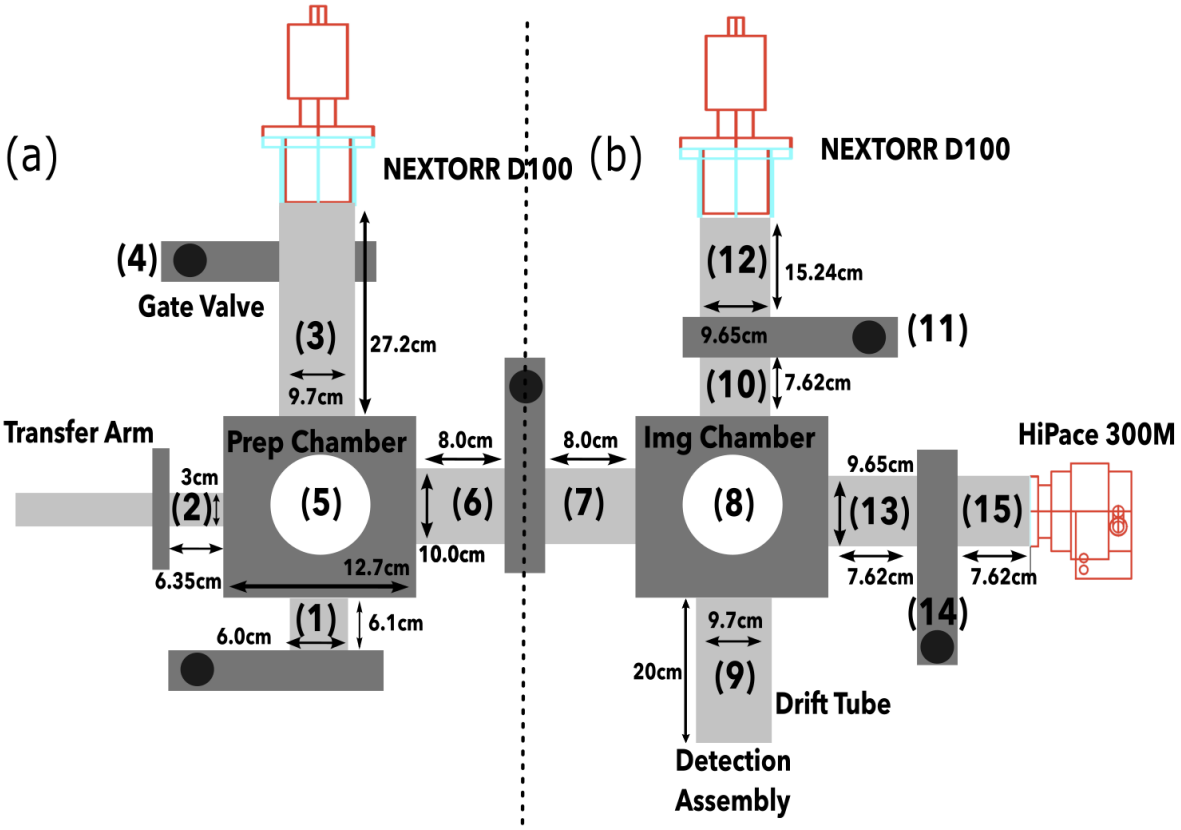

Figure A.1: Diagram of vacuum system, with relevant dimensions marked. Dotted line shows demarcation where region (a) and (b) can be isolated by an in-line valve.

Below we show the results of system volume, surface areas, and conductance calculations. The conductance values of in-line valves, marked with a $*$, were obtained from the Kurt J Lesker website.

Table A.1: System Volumes, Surface Areas, and Conductance

Chamber	No.	Volume (liters)	Surface Area (cm^2)	Conductance (liter/s)
Prep	1	0.172	143	428.5
	2	0.179	148	412
	3	0.469	829	406
	4	NA	NA	1726*
	5	5.9	1712	1000[1]
	6	0.628	329.9	1512
Total		**7.348**	**3162.9**	**112.54**
Imaging	7	0.628	330	1512.5
	8	5.9	1712	1000[1]
	9	0.739	379	1104
	10	0.557	230	1427
	11	NA	NA	1726*
	12	1.114	461	713
	13	0.557	230	713
	14	NA	NA	1726*
	15	0.557	230	713
Total		**9.495**	**3572**	**133.77**

Inputting the calculated values into VacTran we obtain the following pump down estimates, where we consider the entire system as one, shown in Fig. A.2.

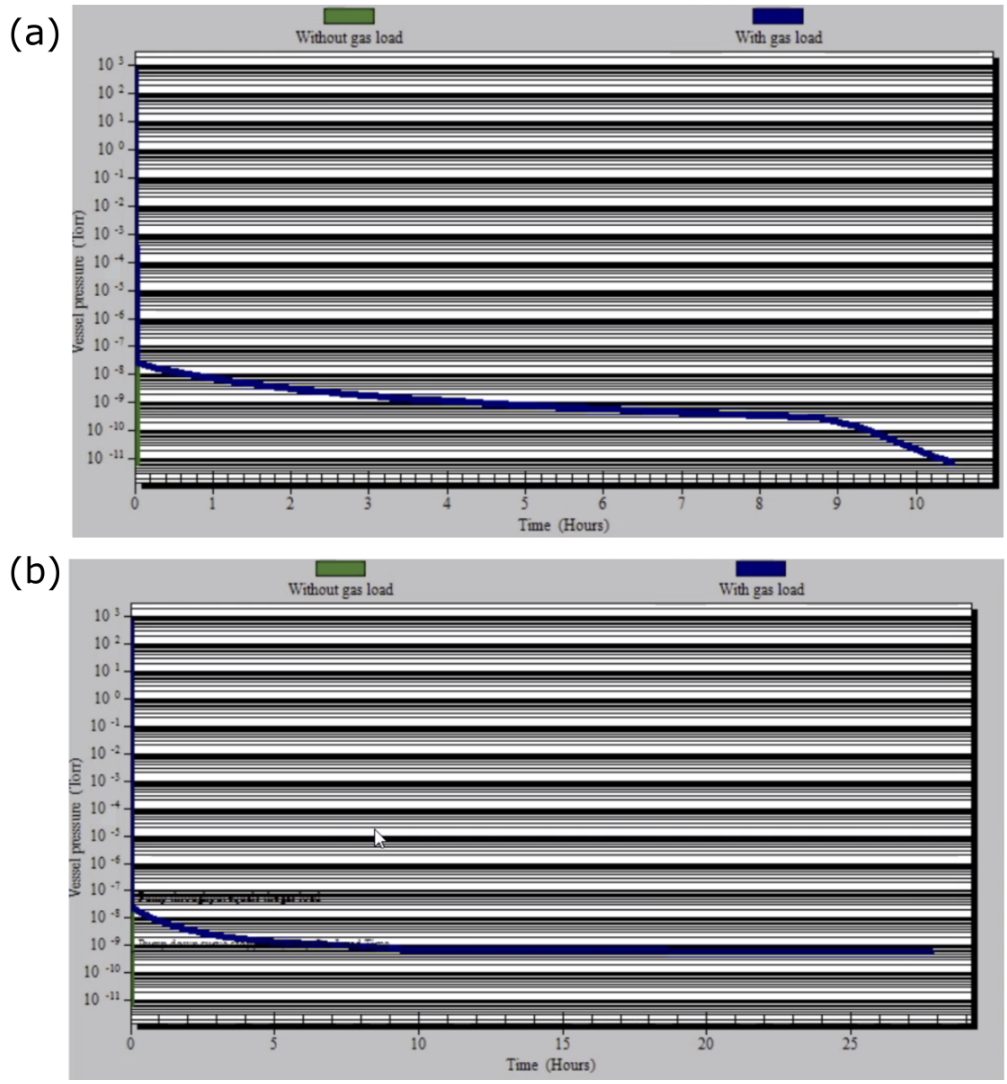

Figure A.2: Vacuum pressure vs time in hours for (a) hydrogen permeation set to 0, and (b) hydrogen permeation set to $\approx 10^{-16}\frac{\mathrm{m}^2}{\mathrm{s}}$. Plots produced using Vactran simulation software.

In Fig. A.2 (a) we show the pump-down time for a system with no permeation, where it predicts it will take approximately 10.5 hours to reach a pressure of 10^{-11} Torr. Fig. A.2 (b)

shows the same results for a system with the expected hydrogen permeation rate of $10^{-16}\frac{\mathrm{m}^2}{\mathrm{s}}$. Here after 25 hours we expect to reach a final pressure of 6x10^{-10} Torr, well into the UHV regime. Similarly, if this rate were set to $10^{-17}m^2/s$, one order of magnitude less than our predicted value, we expect a pump down time of 15 hours to reach a pressure of 10^{-10} Torr.

Overall, there are many more parameters which can be tweaked within the software and it will require updating with the latest information when the final design is completed.